



# BACCHUS

**Impact of Biogenic versus Anthropogenic emissions on Clouds and Climate: towards a Holistic UnderStanding**

Collaborative Project

SEVENTH FRAMEWORK PROGRAMME  
ENV.2013.6.1-2

Atmospheric processes, eco-systems and climate change

Grant agreement no: 603445

<b>Deliverable number:</b>	<b>D1.4</b>
<b>Deliverable name:</b>	Finalized BACCHUS aerosol/cloud data base and documentation (description of the contents)
<b>WP number:</b>	1
<b>Delivery date:</b>	Project month 48 (30/11/2017)
<b>Actual date of submission:</b>	30/11/2017
<b>Dissemination level:</b>	PU
<b>Lead beneficiary:</b>	TROPOS
<b>Responsible scientist/administrator:</b>	A. Ansmann, M.C. Facchini
<b>Estimated effort (PM):</b>	223.13
<b>Contributor(s):</b>	Z. A. Kanji (ETHZ), J. D. Atkinson (ETHZ), J. Bühl (TROPOS); P. Herenz (TROPOS), A. Welti (TROPOS), E. Hashimshoni (HUJI), D. Rosenfeld (HUJI); D. Giguzin (HUJI), G. Roberts (CNRS-GAME), R. Calmer (CNRS-GAME); L. Sogacheva (FMI), S. Decesari (CNR-ISAC), M. Paglione (CNR-ISAC), M. Rinaldi (CNR-ISAC), M. Pikridas (CYI), K. Oikonomou (CYI), K. Savvides (CYI), J. Stavroulas (CYI), P. Antoniou (CYI), N. Mihalopoulos (CYI), J. Sciare (CYI), M. Vrekoussis (CYI), C. Keleshis (CYI), M. Pikridas (CYI), K. Fossum (NUIG), J. Ovadnevaite (NUIG), J. Preissler (NUIG), C. O'Dowd

<b>Contributor(s) continued:</b>	(NUIG), U. Baltensperger (PSI), M. Berto (PSI), J. Dommen (PSI), C. Hoyle (PSI), G. Motos (PSI), R. Pileci (PSI), J. Schmale (PSI), R. Mamouri (CUT), M. Simon (UOF), J. Schrod (UOF), H. Bingemer (UOF), J. Curtius (UOF), R. Rosberg/F. Malkemper/J. Kosmann/S. Hack/J. Drücke/M. Jesswein/A. Haunold/C. Hartwick/N. Koch/D. Machill (UOF), Stephany Mazon (UHEL), Antti Manninen (UHEL), Bjarke Moolgard (UHEL), Georgios Fanourgakis (UOC), S. Fiedler (MPI-M), D. Tonev (INRNE), I. Kalapov (INRNE), C. Angelov (INRNE), T. Arsov (INRNE), A. Boyagjieva (INRNE), C. Ivanov (INRNE), A. Tofaris (UMAN)
<b>Estimated effort contributor(s) (PM):</b>	ETH=2 PM, TROPOS=27 PM, FMI=2.37 PM, HUJI=16 PM, CNRS-GAME=16 PM, CNR-ISAC=24 PM, MPI-M=10 PM, CYI= 31.8 PM, NUIG= 14 PM, PSI= 17.4 PM, CUT= 3 PM, UOF= 9.96 PM, UHEL= 14 PM, UOC = 6.6 PM, INRNE=23 PM, UMAN=6
<b>Internal reviewer:</b>	Ulrike Lohmann, Monika Burkert

## **Finalized BACCHUS aerosol/cloud data base and documentation (description of the contents)**

Work package 1 (WP1) covers the aerosol and cloud observations performed within the framework of BACCHUS. Focus is placed on the characterization of aerosol particles to serve as cloud condensation nuclei (CCN) and ice-nucleating particles (INP) based on past and published in-situ measurements, as well as those from new observations (e.g., BACCHUS, Mace Head 2015, Cyprus campaigns, 2015-2018). The goal is to establish a global database or database infrastructure (which does not necessarily contain the data physically) of CCN and INP properties for different natural and anthropogenic aerosol types and mixtures around the world. WP1 also deals with vertically resolved field observations of aerosols and clouds in key climate regions with aerosol/cloud lidars and cloud radars, organized in networks (e.g., ACTRIS, Cloudnet) or arranged in super sites within large field campaigns (e.g., BAECC, CyCARE), and by including aircraft observations (e.g., ACCACIA, ACRIDICON). Spaceborne observations with focus on aerosol-cloud interaction is also included in the BACCHUS activities. As a unique contribution satellite remote sensing with very high horizontal resolution is used to study aerosol-cloud-dynamics relationships in key regions of global climate and climate change.

In the first phase of the BACCHUS project period, closure studies, validation efforts, quality assurance work and re-analysis of past observations were performed. Most of these efforts were successfully completed after 24 months, several after 36 months. Here, we report some highlights of observations of aerosol-cloud interactions performed in the framework of Task 1.5 during the last 12 months. Tasks 1.1 – 1.4 were completed after 36 BACCHUS project months (with final results in WP1 deliverable D1.3). Task 1.6 is mostly based on the surface observations of CCN and INP concentrations performed within Tasks 1.1-1.4. The final status of the INP data base (Task 1.6) is discussed at the end of this report.

To provide an overview, WP1 is organized in the following six tasks:

**Task 1.1:** Definition of the natural background aerosol and measurement framework for the IN database

**Task 1.2:** Compilation of geographic differences in INP/CCN

**Task 1.3:** Quantification of natural (biological, dust) and anthropogenic contributions to INP

**Task 1.4:** Quantification of biogenic and anthropogenic contribution to organic aerosol and their ability to act as CCN

**Task 1.5:** Obtaining the vertical structure of aerosols and clouds

**Task 1.6:** Establishment of a harmonized dataset of aerosol, CCN/INP and cloud microphysical properties

The goal of Task 1.5 is to investigate aerosol-cloud interaction in the boundary layer (mostly liquid-water cloud layers) and in the free troposphere (here the focus is on mixed-phase cloud layers). These observations (case studies, general findings) can be used by the BACCHUS modelling groups. A few highlights from satellite remote sensing (HUJI, FMI) are presented in Sections 1 and 2. Progress in the analysis of Cloudnet observations (TROPOS, vertical profiling of clouds and aerosol, now fully including the Barbados station of MPI-M) is reported in Section 3. Contributions to the field research of aerosol-cloud interactions based on measurements aboard unmanned aerial vehicles (UAVs) are given in Section 4 (CNRS-GAME). Section 5 summarizes the Task 1.6 activities with the final status of the BACCHUS ice nucleation data base.

## **1 Studies of aerosol-cloud interaction (liquid-water clouds) in pristine and polluted environments (HUJI)**

We present a few representative results to highlight the impact of man-made aerosol pollution on microphysical properties of clouds. The results are taken from the master thesis of Eyal Hashimshoni (HUJI). The retrieval of CCN concentrations at cloud base of convective clouds is based on the technique described in Rosenfeld et al. (2016). The method mainly relies on the data products of the Visible Infrared Imaging Radiometer Suite (VIIRS) passive sensor, onboard the Suomi National Polar-orbiting Partnership (NPP) satellite. Suomi-NPP is a sun-synchronous polar-orbiting satellite that overpasses at 13:30 solar time. The VIIRS sensor has a very high spatial thermal resolution of 375 meters at nadir that is useful for detecting small cloud elements. VIIRS products can be utilized to produce maps of cloud microphysical properties [Data are available at [https://www.class.ngdc.noaa.gov/saa/products/search?sub\\_id=0&datatype\\_family=VIIRS\\_SDR&submit.x=29&submit.y=4](https://www.class.ngdc.noaa.gov/saa/products/search?sub_id=0&datatype_family=VIIRS_SDR&submit.x=29&submit.y=4)].

A new methodology is utilized to produce automated maps of retrieval of microphysical properties of convective cloud fields over large areas. The recently developed Automatization Mapping of Convective Clouds (AMCC) system enables to investigate natural and man-made causes on large scales. In order to produce the AMCC, a scene of satellite image of about 2400x2304 km is undergoing image segmentation to pixels of 36x36 km. The microphysical properties are retrieved for each moving window using the satellite retrievals. Afterwards, cirrus screening mechanism is applied to filter out cirrus clouds. Then, quality control is applied in order to filter out further clouds with elevated bases and pixels with extreme satellite zenith angles. At last, the whole image is graphically visualized by MATLAB software.

The methodology to retrieve CCN from satellites by using clouds as CCN chambers has been validated against ground measurements in Europe and the Americas. Satellite-retrieved CCN was also compared against ground measurements from the atmospheric observatories of the Aerosols, Clouds, and Trace gases Research Infra-Structure (ACTRIS). Data are analyzed from European stations located at higher latitudes at Cabauw (Netherlands), Mace Head (Ireland), Vavihill (Sweden) and Hytiälä (Finland). While the method still requires improvements (especially at high latitudes), it has already become useful as a research tool at lower latitudes. The latest development of AMCC enables us to investigate and produce spatial maps of CCN. This capability was exploited to infer the CCN regime in pristine like environments, a feature that is crucial to improve understanding of aerosol-cloud-interactions.

This study uses the spatial data provided by the AMCC to analyze first the CCN and other microphysical properties of pristine environments. A case is presented in Section 1.2. Section 1.3 then discusses two pollution cases. The cases were analyzed in two ways: First, CCN retrievals from the AMCC method were overlaid upon simulated CCN maps under fixed water supersaturation (S) based on the WRF 3.4/CMAQ 5.01 coupled modeling system. Secondly, backward trajectories from the Hybrid Single Particle Lagrangian Integrated Trajectory Model (HYSPLIT) model (data are available at <http://ready.arl.noaa.gov/HYSPLIT.php>) were overlaid upon the CCN retrieved spatial maps to analyze the temporal changes in CCN in clean and near perturbed environments. The trajectory analysis is analogous to the flow of air with time until reaching the endpoint of the trajectory. The endpoint of the trajectory height input is 500 meters, so it represents air parcels within the boundary layer. To receive the cross-section of CCN(S), cloud base temperature (Tb), S, and updraft velocity at cloud base (Wb) along the trajectory, each trajectory point is related to the microphysical value of the closest pixel. Furthermore, in order to decrease noise and bias, averaging of the microphysical values is applied on the neighboring points in a rectangle surrounding the trajectory point with width of 1° (perpendicular to the trajectory azimuth) and with length that covers a distance that

corresponds to 1:30 hours before and 1:30 hours after the trajectory point (parallel to the trajectory azimuth).

## 1.2 Pristine environments

The Amazon basin is investigated in this section as an example of an unperturbed environment, since it is assumed to maintain pristine conditions during the rainy season from January until June. The Amazonian basin is usually characterized by north-eastern flow of the trade winds from the Atlantic Ocean inland. The flow brings clean air masses subsiding from the Azores high area. Distribution maps of microphysical properties at Green Ocean Amazon during 16/7/2014 17:12 UTC along with a cross-section of a HYSPLIT based backward trajectory are presented in Fig.1.1. Important features of pristine environments might be interpreted from this case study. Based on Fig. 1.1c-d it can be seen that convective unperturbed clouds display low CCN concentration of about  $50 \text{ mg}^{-1}$  and S of up to 1% above the Ocean. As air parcels move inland, the CCN concentration rises sharply at the shore until it stabilizes at values of about  $200 \text{ mg}^{-1}$ , while S decreases respectively to values of less than 0.5%. Due to rain formation, CCN concentration can decrease inland. In the Green Ocean Amazon, low CCN concentrations cause efficient precipitation scavenging, which reduces CCN concentrations. This phenomenon might occur 500-800 km inland from shore. Precipitation is probable in this area due to the large depth of clouds observed. Along the trajectory, Wb (which is proportional to cloud base height Hb) increases gradually inland, suggesting some contribution of meteorological processes to the increase in droplet concentration Nd. Tb is warmer and Wb is weaker over the ocean, where humidity supply is larger and sensible heat fluxes are weaker. Above land, air is usually warmer and drier at noon, leading to stronger Wb and colder Tb as air moves inland. Similar studies were performed in southeastern Australia (as part of the master thesis of Eyal Hashimshoni) and confirmed the results obtained over northeastern Brazil.

## 1.3 Anthropogenic aerosol perturbations

In order to obtain a comprehensive review regarding CCN perturbations, heavily populated environments were also examined. First, the area of southern Texas was analyzed during 07/06/2014 19:34 UTC, as shown in Fig. 1.2. In this case, southeast wind flows from the Gulf of Mexico to the Gulf Coast of Texas and Louisiana and then veers to southwest direction inland. It appears that this area is polluted both over the ocean and inland. In contrast to pristine marine conditions, in Fig. 1.2c there are clouds over water that have CCN concentration of up to  $700 \text{ mg}^{-1}$ , potentially due to ships or due to emissions of the large oil industry found at deep sea. The CCN concentration in this case study increases inland when the spatial distribution of CCN inland is varied. Over the large cities of Houston and New Orleans (both having numerous oil refineries) CCN concentration can exceed  $2000 \text{ mg}^{-1}$ , while rural areas exhibits lower CCN concentration of about  $200-400 \text{ mg}^{-1}$ . Since the coastal area has similar Wb along the coast, it is very likely that the aerosol emissions are the reason for high CCN concentration close to large cities. In contrast to the Australia and Brazil case studies, in Fig. 1.2d the calculated S at cloud base is relatively low both over the ocean and inland and is mostly below 0.4%. In Fig. 1.2a-b it can be seen that Tb decreases and Wb increases more steeply further inland, in agreement with other case studies discussed in the master thesis. Along the trajectory, we see the following: First, the CCN baseline at sea is relatively high ( $150 \text{ mg}^{-1}$ ). Secondly, further away from shore after the pollution plume of Houston ( $1000 \text{ mg}^{-1}$ ), CCN concentration declines to  $300-400 \text{ mg}^{-1}$ , suggesting the impact of aerosol perturbation inland is diluted but not diminished. Thirdly, Wb and CCN trends along the trajectory are not highly correlated, implying a strong net aerosol effect.

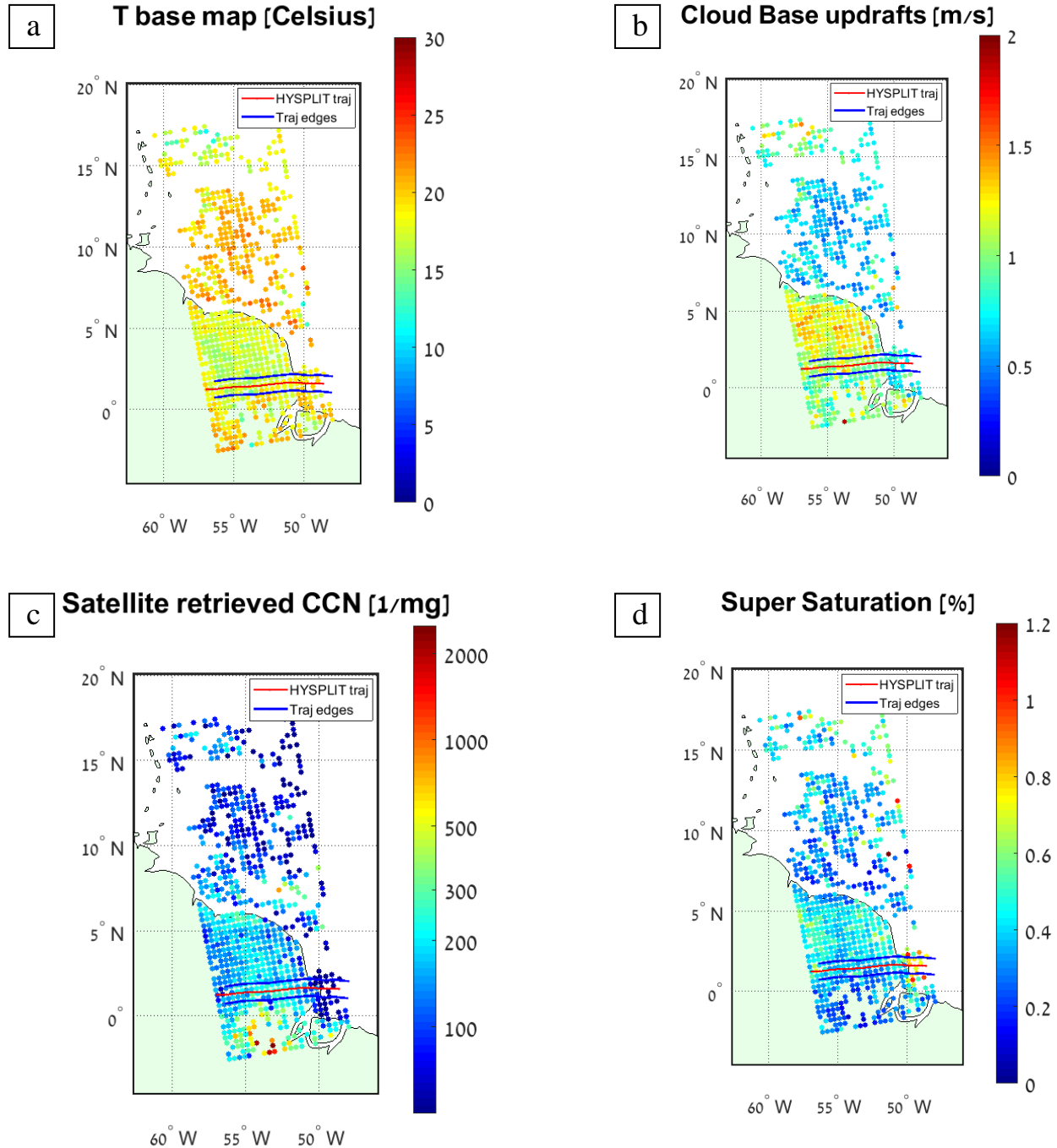


**Figure 1.1:** Pristine case study of liquid-water clouds over the tropical Atlantic and the northeastern part of Brazil (Green Ocean Amazon), 16/7/2014 17:12 UTC. Satellite-retrieved cloud base temperature  $T_b$  [ $^{\circ}$ C] (a), cloud base updraft velocity  $W_b$  [m/s] (b), CCN mixing ratio  $N_{CCN}$  [#/mg] (c, number concentration per mg of air is roughly equivalent to #/ $cm^3$ ) and water vapor supersaturation  $S$  [%] (d) are presented with overlay of HYSPLIT backward trajectory model (red) and 1° width of the trajectory for each side (blue).

Comparison between satellite-retrieved CCN and WRF 3.4/CMAQ 5.01 coupled modeled CCN for this case study is shown in Fig. 1.3. While both methods identify high CCN concentration above Houston, Lake Charles, Dallas and New Orleans, the satellite retrieval identifies pollution patterns at 34° N, 96° W that are not identified by the model. Differences

in the CCN patterns and the absolute concentrations are also apparent. The satellite-detected pollution plumes are more widespread, in contrast to narrower and more local pollution plumes analyzed by the model.

The most severe anthropogenic polluted conditions found on Earth can be observed above the area of eastern China. Comparison between the satellite retrieved CCN and the WRF 3.4/CMAQ 5.01 coupled modeled CCN is presented in Fig. 1.4 for the 16/06/2015 at 05:41 UTC during southern winds regime. In this case, the overall land area is heavily polluted, so that satellite-retrieved CCN concentrations are between 500 to more than 2000 mg<sup>-1</sup> over most of the continent. In contrast, the model has a more limited dispersion of the anthropogenic related pollution, since some low aerosol pockets are observed inland. Furthermore, over the South China Sea the satellite retrieval estimates high CCN concentration of up to 500 mg<sup>-1</sup> in comparison to values of less than 100 mg<sup>-1</sup> calculated by the model.

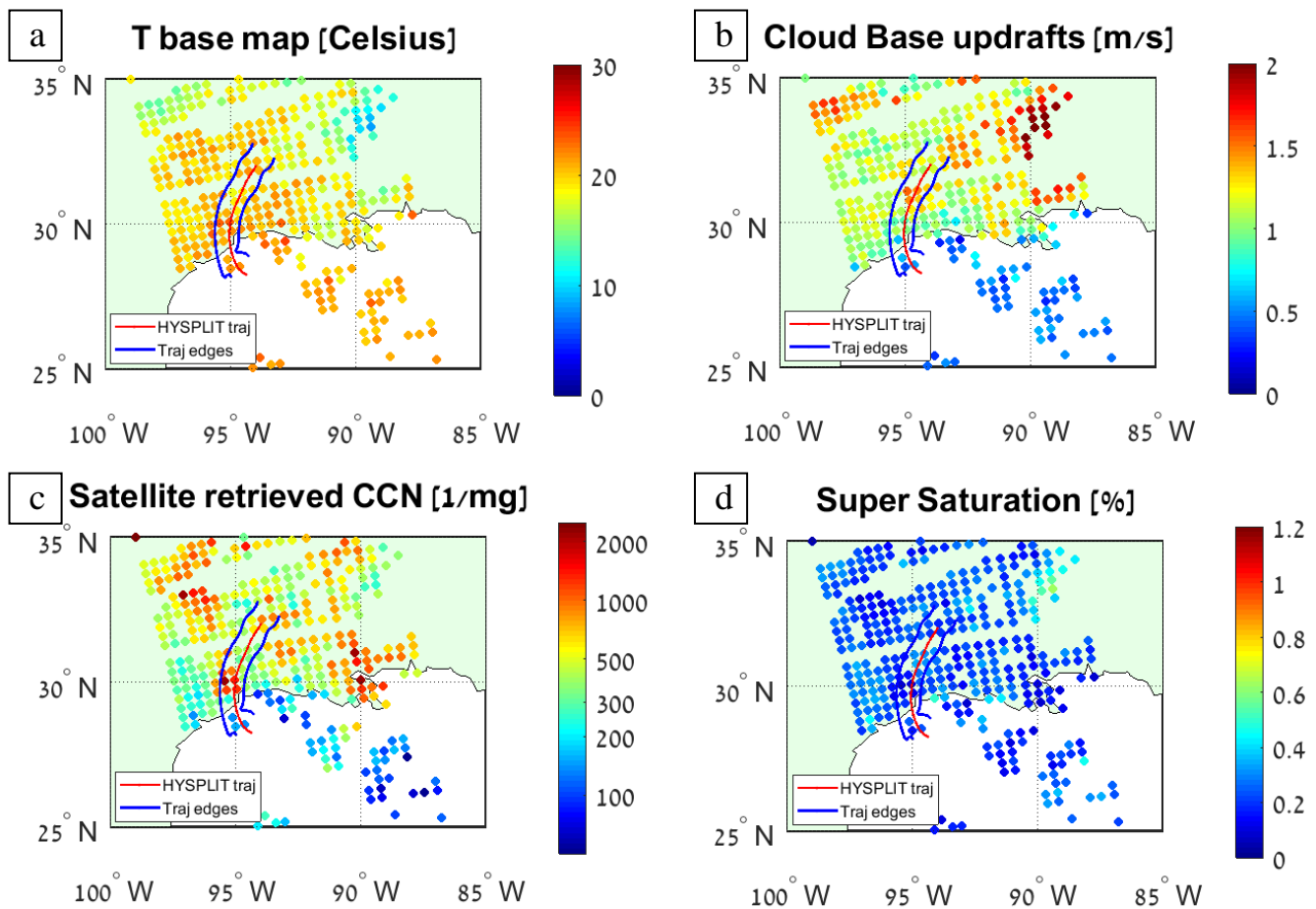


**Figure 1.2:** Case study of liquid-water clouds over southern Texas and the Gulf of Mexico, 07/06/2014 19:34 UTC. Satellite-retrieved  $T_b$  [ $^{\circ}$ C] (a),  $W_b$  [m/s] (b),  $N_{CCN}$  [#/ $mg$ ] (c) and  $S$  [%] (d) are presented with overlay of HYSPLIT backward trajectory model (red) and 1° width of the trajectory for each side (blue).

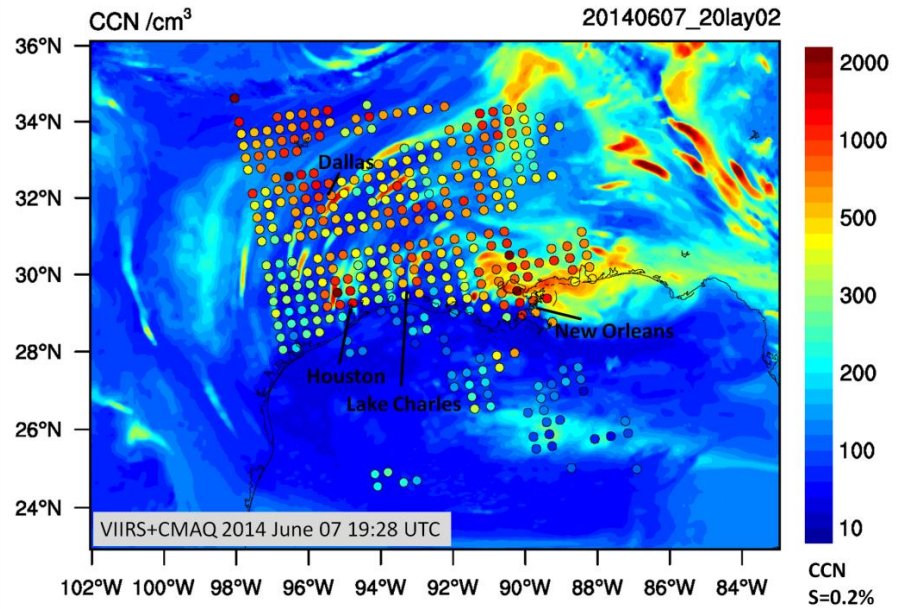


**Figure 1.3:** Comparison between satellite-retrieved CCN (dots) and WRF-3.4/CMAQ-5.01-coupled modeled CCN under  $S$  of 0.2% at 20:00 UTC (filled contours) for case study over southern Texas, 07/06/2014 19:34 UTC. The color scale is in units of #/mg for the satellite and in units of #/cm<sup>3</sup> for the model. Cities with large industrial centers are named on the map.

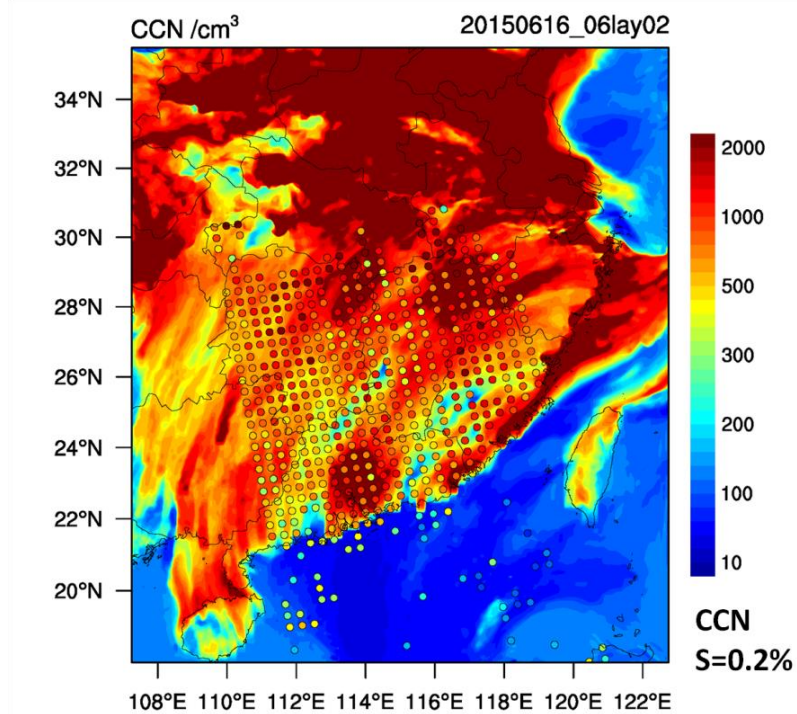


**Figure 1.4:** Comparison between satellite-retrieved CCN (dots) and WRF-3.4/CMAQ-5.01-coupled modeled CCN under  $S$  of 0.2% at 06:00 UTC (filled contours) for case study over southern China, 16/06/2015 05:41 UTC. The color scale is in units of #/mg for the satellite and in units of #/cm<sup>3</sup> for the model.

In summary, we found that in unperturbed environments such as the Green Ocean Amazon and Southeast Australia CCN spatial distribution patterns are similar, meaning pristine-like environments could still be found at continents and not only at remote oceans. Over oceans, convective clouds show very low concentrations of CCN varying from  $20\text{-}100 \text{ mg}^{-1}$ . CCN concentration increases at the shore probably due to the abundance of biogenic related aerosols at the continent, and continue to increase inland until stabilizing at values of  $100\text{-}200 \text{ mg}^{-1}$ . Precipitation scavenging might lead to a reduction of CCN both over ocean and inland. Increase in CCN in these environments is usually accompanied by a decrease in S at cloud base. As clouds move inland Wb is enhanced and Tb becomes colder. However, synoptic conditions and topography might also change Wb and Tb inland. Natural aerosol perturbations in pristine environments can have a large impact on CCN concentration, which in turn might affect cloud properties, precipitation rate and cloud radiation interactions. As an example, the area of Roraima located in the Amazon basin appears to be subjected to occasional wildfires that increase CCN concentration above this area dramatically. Aerosol perturbations seem to be less significant when an area is already influenced by human activities. In areas when sporadic emission sources exist such as the southern coast of Texas, CCN concentrations increase close to emission sources. Background CCN concentration inland is calculated to be about  $400 \text{ mg}^{-1}$ , which is by a factor of 2 higher than in pristine environments inland. In heavily polluted areas such as southern China, the impact of specific aerosol emission sources such as a major city on cloud properties is almost unnoticeable, since the background CCN concentration is already very high ( $> 1000 \text{ mg}^{-1}$ ).

This study has also shown that a comparison of satellite retrievals and WRF 3.4/CMAQ 5.01 coupled model can shed light on the advantages and disadvantages of the satellite retrievals. It appears that while large pollution sources are detected by both methods, every approach is still imperfect. The WRF 3.4/CMAQ 5.01 model seems to fail in detecting fires and their related aerosol emissions. It is biased since it is based on assumptions regarding emissions inventories. On the other hand, the satellite retrievals still have some shortcoming related to multilayer screening of clouds and to underestimation of CCN in shallow marine precipitating clouds.

In order to reconstruct the pre-industrial era CCN regime, the next important step in this process could be to create a statistical analysis of microphysical properties and the cloud radiative effects for various pristine environments in different meteorological conditions. Along with building similar methodologies and databases for different types of clouds, the understanding of aerosols-cloud interactions might be improved by far. This study and possible future research embodies progress that could potentially lead to a better understanding of the radiative forcing of aerosol-cloud interactions and by that to improve predictions for climate changes.

## 2 Aerosol-cloud interaction studies based on AATSR observations (FMI)

### 2.1 Introduction

Aerosol optical depth (AOD) and cloud parameters retrieved using top of atmosphere (TOA) radiances measured by the Advanced Along Track Scanning Radiometer (AATSR) were used to investigate their spatio-temporal variations and the effects of aerosol particles on cloud properties in five regions characterized by different aerosol conditions.

Aerosol particles are known to affect the formation of clouds. Changes in aerosol composition and concentration lead to changes in the number concentration and size of cloud droplets that influence the lifetime and reflectivity of clouds. Anthropogenic aerosol particles may influence cloud formation through two mechanisms. One is the effect on cloud microphysics by forming smaller and more numerous cloud droplets with increasing aerosol concentration for constant liquid water path (Twomey, 1997), thus reducing precipitation and, as a consequence, presumably enhancing cloud lifetime. The second effect is referred to as the aerosol dynamic-hydrological effect in which the aerosol direct, semi-direct, and indirect effects can modulate atmospheric radiation, leading to redistributions of clouds and precipitation (Takemura et al., 2007). Some aerosol types suppress cloud formation and precipitation (Rosenfeld, 2000; Koren et al., 2004). Other aerosol types can enhance precipitation or have opposite effects on precipitation over land and ocean (e.g., Jiang et al., 2013). To assess the effect of aerosol particles on regional and global climate change, detailed information is required on their concentrations in different regions in the atmosphere.

The major sources of aerosol particles in the atmosphere are desert dust, smoke from biomass burning, sea spray aerosol, and anthropogenic particles from direct emissions and secondary aerosol particles formed from precursor gases emitted due to human activities. Desert dust is a major natural source of atmospheric aerosol particles that can potentially affect clouds. It is probably a less potent aerosol for suppressing precipitation than is smoke from burning vegetation. However, the vast amounts and regional extent of desert dust in the atmosphere make it an important factor in suppressing potential raindrop formation (Rosenfeld, 2000).

For the simultaneous retrieval of aerosol and cloud properties, the TOA reflectance data from the AATSR have been utilized in the current study. For a description and specifications of the instrument, see <https://earth.esa.int/web/sppa/mission-performance/esa-missions/envisat/aatsr/sensor-description>.

### 2.2 The AATSR retrieval algorithm and study area

The ADV/ASV aerosol algorithm (ADV: AATSR Dual View, ASV: AATSR Single View) for the retrieval of AOD using (A)ATSR dual view radiometers (Kolmonen et al., 2016) has been further developed and tested. The Dual View algorithm provides aerosol data on a global scale with a default resolution of  $10 \times 10 \text{ km}^2$  (L2) and an aggregate product on  $1^\circ \times 1^\circ$  (L3). Optional, a  $1 \times 1 \text{ km}^2$  retrieval product can be made available for specific studies over smaller areas. Since for the retrieval of AOD using ADV no prior knowledge on surface properties is needed, the surface reflectance can be independently retrieved using the AOD for atmospheric correction (Sogacheva et al., 2015). To avoid cloud contamination to AOD, effective cloud screening is needed as the aerosol properties can be retrieved only for cloud-free conditions (Sogacheva et al., 2017).

For cloudy pixels, a semi-analytical cloud retrieval algorithm using backscattered radiation in the 0.4–2.4  $\mu\text{m}$  spectral region has been implemented to ADV/ASV for the determination of the cloud optical thickness (COT), the cloud droplet effective size (Ref), the liquid water path (LWP) and cloud albedo (alb). This cloud retrieval algorithm was originally developed by Kokhanovsky et. al. (2003). It works well for thick clouds with COT>10. A problem for thin cloud retrieval exists due to the surface reflectance contribution to the TOA radiance. The cloud top height (CTH) module for ADV has been developed by Virtanen et al. (2014).

Seasonal and temporal variations in AOD and the impact of these variations on the properties of clouds were examined over five regions, characterized by different aerosol properties. To this end, a database was created with aerosol and cloud optical properties at 1 km-resolution over each of the five regions, for the year 2008. These regions are:

- biomass burning Amazon + Barbados (12.5°S-18°N, 45°W-75°W),
- relatively clean Europe (36°-72°N, 15°W-45°E),
- Saharan dust outbreaks and primary organic sea spray emissions over the Central Atlantic (0°-70°W, 0°-30°N)
- polluted China, with further division for land (25°N -37°N, 110°E-120°E) and ocean (25°N -33°N, 122°E-130°E).

## 2.3 Results and interpretation

### 2.3.1 Time series

The monthly averaged AOD and cloud properties for 2008 are presented in Fig. 2.1. Large differences in both the values and the temporal variation are observed between the five regions of interest. As expected, the highest AOD with minima in winter and increasing AOD towards summer (with a decrease in July, which has to be further studied) is observed over China. Higher levels of AOD values during spring are caused by dust storms over the Taklimakan and Gobi deserts during that season and subsequent transport to the NE of China. In summer, the monsoon influences (depending on its intensity) the AOD and its spatial distribution over China. A correlation analysis of cloud properties with aerosol optical depth over India (Patil et al., 2017) shows that less pronounced monsoon years are characterized by more frequent and larger decreases in cloud drop size and ice water path, but increases in cloud top pressure, with increases in aerosol abundance. The opposite was observed during strong monsoon years. Over China, year-to-year differences in the monsoon intensity are also observed (Luo et al., 2015), thus yearly changes in averaged cloud properties are expected.

An annual cycle of AOD with a minimum in July is also observed in the Atlantic dust area. Spring and autumn maxima related to biomass burning activity are observed over the Amazon, where the following seasonal influences affect aerosol concentrations and composition: (i) the wet season is typically between February to May and shows the cleanest atmospheric state, (ii) the transition period from wet to dry season is typically between June and July, (iii) the dry season months from August to November show the highest pollution levels, and (iv) the transition period from dry to wet season is December and January (Andreae et al., 2015). The lowest AOD with a less pronounced yearly cycle with some (ca. 0.1) increase in AOD in spring and fall is observed over Europe.

Clear minima in COT occur over China (both land and ocean, Figure 2.1) in summer, when (except for July) AOD is higher compared to other seasons. Similar effects have been observed with MODIS (Liu et al., 2017). This strongly implies that the changes in COT are caused by changes in aerosol loading conditions. At the same time, Ref increases with AOD exceeding a threshold of approx 0.35. This phenomenon was studied recently for this particular region by Liu et al. (2017) for warm clouds. They concluded that for AOD values up to 0.35 the usual Twomey effect was detected where Ref was decreasing with increasing aerosol loading. For higher AOD values Ref increased but COT decreased with increasing AOD. Liu et al. (2017) concluded that these effects may be caused by microphysical processes together with vapour competition and evaporation of small droplets due to high abundance of aerosol particles. Over China, there are more stratiform clouds, especially stratocumulus, in winter than in summer. The wintertime low-level convergence and mid-level divergence prohibit deep convection, and thus high clouds cannot form. In contrast, high

clouds are prevalent in summer, especially cirrus and deep convective clouds (Guo and Zhou, 2015).

For the Amazon and Europe, summer minima in COT are less pronounced. In the Amazon area COT and Ref roughly follow the Twomey effect (Fig.2.1). In Europe, there is no notable yearly cycle in AOD and, thus, the cloud parameter variations cannot be explained based on the monthly variations in aerosol loading. Also, it must be noted that the spatial satellite coverage over Europe varies significantly throughout the year as no retrievals are possible over the northern part of the region due to the lack of sunlight during the local winter season. Over the Atlantic, COT is almost constant during the whole year, as for AOD.

The cloud droplet effective radius and LWP show a clear yearly cycle with maxima in summer and minima in the winter period over China, which may partly be explained by the effects of the monsoon (Li et al., 2016). In contrast to China, the rainy season in the Amazon occurs in the winter (Li et al., 2006, Martins et al., 2015). The highest Ref and LWP occur over polluted biomass burning areas in China and the Amazon, e.g. in the areas, where the highest AOD loadings are observed. Similar relations between AOD and Ref over China has been discussed in Tang et al. (2014), who also suggested that the influence of background weather conditions need to be considered when studying the interactions between aerosol and cloud.

Cloud albedo behaves similar as COT and decreases towards the summer months for most of the regions, except the Atlantic, where the yearly cycle for albedo is almost flat throughout the year with a small peak in the winter. CTH increases during the summer over China but decreases over the other regions. The annual cycle of cloud fraction is similar to the annual cycle of rainy seasons in each region and depends on aerosol loading (Liu et al., 2017). Cloud fraction is decreasing towards summer months over Europe and Amazon, while for China spring and autumn minima can be recognized.

### 2.3.2 Relations between AOD and cloud properties

The analysis of the scatter plots for aerosol and cloud properties (Fig. 2.2) confirms the differences in AOD in clean and polluted environments and reveals the effect of aerosol particles on COT and Ref (and, thus, cloud albedo). Polluted clouds over China have higher COT and smaller cloud droplets and, thus, a higher cloud albedo. For AOD up to ca. 0.4, both Ref and COT decrease, but for higher AOD Ref increases with increasing AOD while COT continues to decrease (Liu et al., 2017). A similar tendency is observed over Europe. However, monthly averaged COT values over Europe are in the range of 14-21, while for China over ocean COT is almost reaching a value of 40.

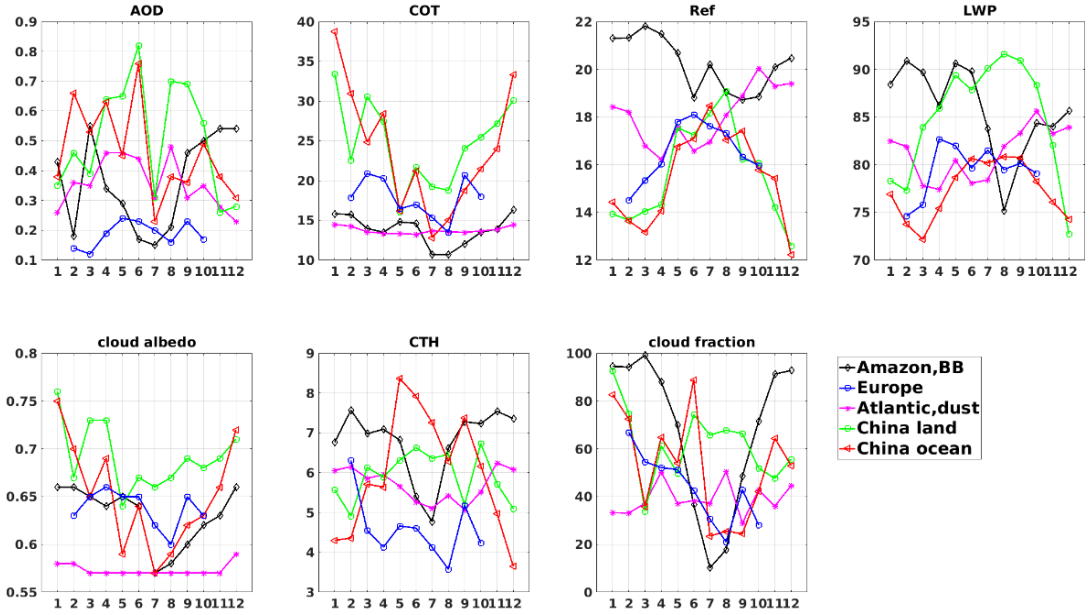


**Figure 2.1:** Yearly cycle for aerosol (AOD) and cloud (COT, Ref, LWP, cloud albedo) properties, Cloud Top Height (CTH) and cloud fraction over areas with different aerosol and cloud properties and regimes: biomass burning Amazon (black), central Atlantic dust region (purple), polluted China land (green) and ocean (red), and less polluted Europe (blue) for year 2008.

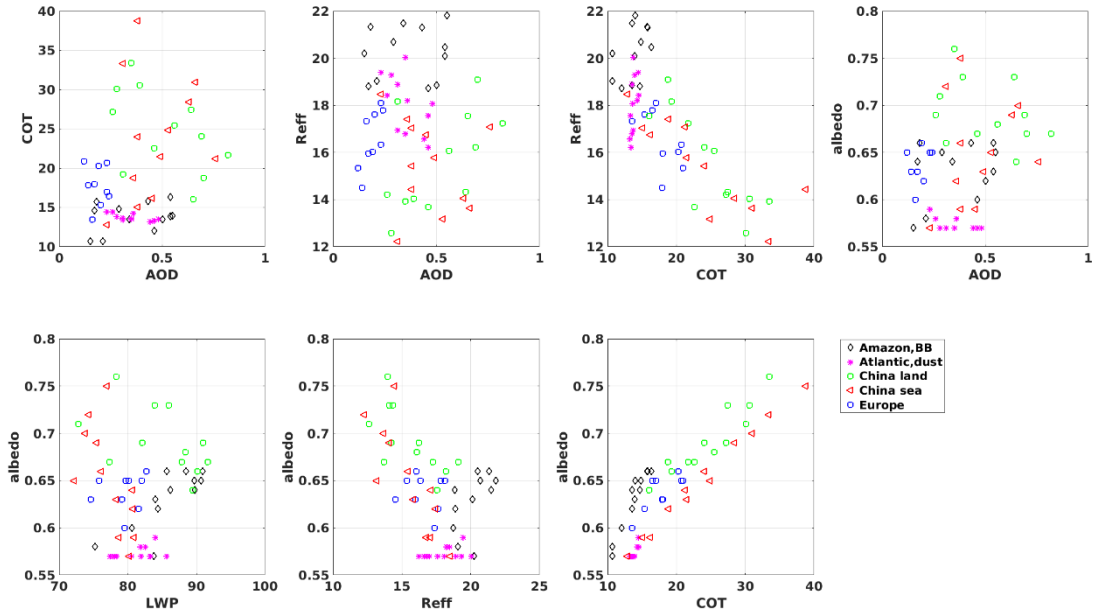


**Figure 2.2:** Scatter plots for aerosol (AOD) and cloud (COT, Ref, LWP, cloud albedo) properties, over areas with major aerosol types: biomass burning Amazon (black), central Atlantic dust region (purple), polluted China land (green) and ocean (red), and less polluted Europe (blue) for year 2008.

The relationships (cross-correlation) between monthly, seasonally and yearly aggregates of AOD and cloud parameters (for year 2008) in the five study regions have been analyzed. Results for seasonal and yearly aggregates are shown in Table 1a-e, Supplement.

For the Amazon region (Table 1Sa), biomass burning aerosol dominates the mean annual aerosol optical thickness. The dry season, which occurs from July to December, is the period that faces higher biomass burning emissions. A maximum correlation between AOD and COT (0.25) is observed in winter. The highest correlation over the year (0.57) was observed between AOD and cloud fraction (CF). The reason for that is twofold. First, at certain conditions, aerosol particles often act as Cloud Condensation Nuclei (CCN), on which cloud droplets are formed. Second, a twilight zone exists, which is a belt of forming and evaporating cloud fragments and hydrated aerosols, which may extend to tens of kilometers from the clouds to the so-called cloud-free zone (Koren et al., 2007).

Over Europe (Table 1Sb), where the aerosol distribution is determined by different aerosol types (marine, polluted, biomass burning, pristine, transported dust), the correlation between AOD and CF over the year was lower (0.37). Over mainland China (Table 1Sc), where strongly polluted aerosol particles together with dust are the main aerosol types over land, the correlation between AOD and CF was also low (0.33 over the year). A correlation ( $R$ ) of 0.41 has been obtained between AOD and CF over the East China Sea (denoted as China, ocean in Table 1Sd).

The strongest relationship between AOD and cloud properties has been revealed over the Atlantic – the area, which is strongly influenced by the primary organic sea spray emissions, which might act as CCN (Westervelt et al., 2012) and episodic and seasonal strong Saharan dust transport events (van der Does et al., 2016). Finer grained dust particles are observed during winter and spring, and coarser grained particles are observed during summer and fall (van der Does et al., 2016). Over the Atlantic (Table 1Se), a rather good correlation (0.46 over the year) is observed between AOD and LWP, reaching its maxima (0.57) in summer. The correlation is lower between AOD and Ref (0.34).

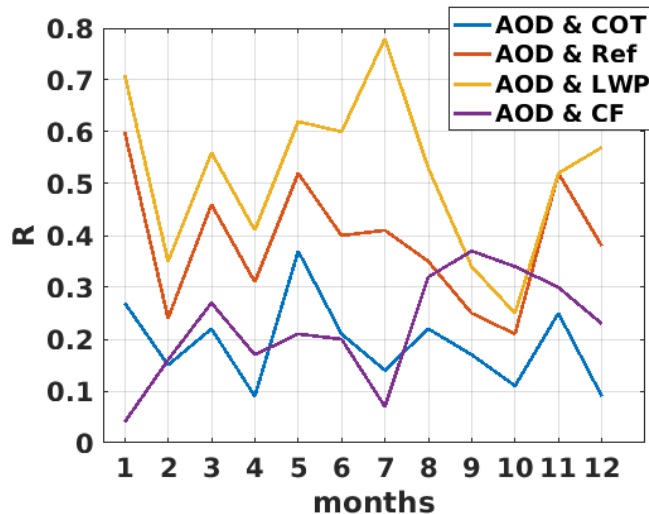


**Figure 2.3:** Monthly correlation ( $R$ ) between AOD and COT (blue), Ref (orange), LWP (yellow), CF (purple) over the Atlantic in 2008.

For the Atlantic, we also show the monthly variation of the correlation coefficient ( $R$ ) between COT, Ref, LWP, CF and AOD (Fig. 2.3).  $R$  shows a similar temporal variation for COT, Ref, LWP and AOD, except in the summer (July), when the correlation between LWP and AOD reaches its maximum (0.78), while the other correlation coefficients remain smaller.  $R(CF\&AOD)$  is highest during the spring and autumn with somewhat lower correlation in the summer.

### 2.3.3 Separation of different LWP regimes for different seasons

For the Atlantic region, we also studied cross-correlations between AOD, COT, Ref, LWP, albedo (alb), CTH and CF for different LWP ranges ( $0-25-50-75-100 \text{ g/m}^2$ ) and for different seasons as well as for the whole year 2008. The results are presented in Table 2S, a-d). For the whole year, there is a strong correlation (0.99) between COT and cloud albedo for  $LWP < 50 \text{ g/m}^2$ , with somewhat lower values (0.92-0.93) for  $LWP > 50 \text{ g/m}^2$ . Scatterplots of albedo vs COT presented in Fig. 2.4 clearly show the separation between COT and albedo for different LWP ranges and only some small differences between the seasons. For instance, in winter (DJF), for the same LWP range (25-50 g/m<sup>2</sup>), somewhat higher COT and albedo values occur. However, there are no significant differences between the correlation coefficients (cf. Table 2S, a-d).

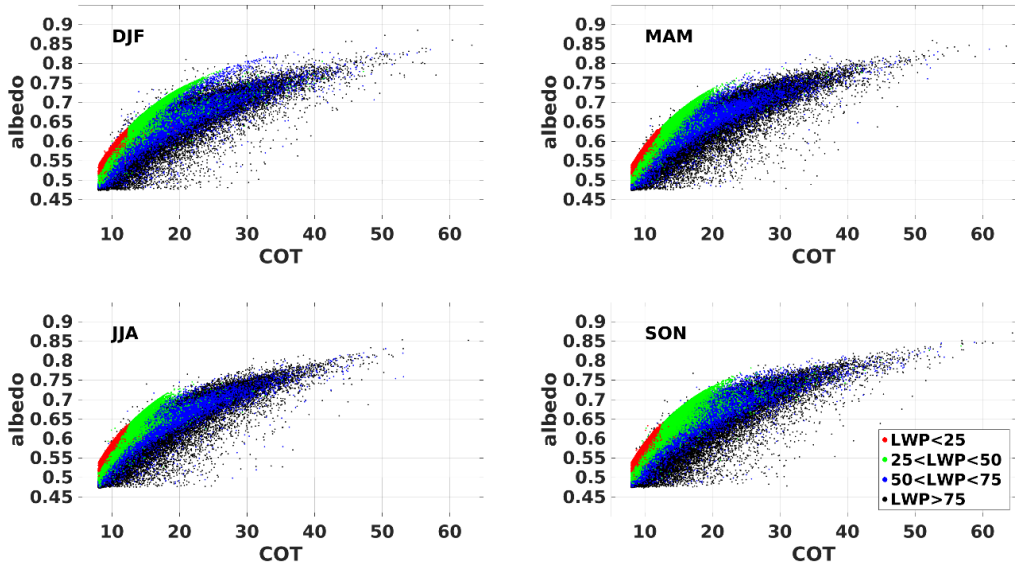


**Figure 2.4:** Scatterplots of albedo vs COT for each pixel different LWP ranges ( $\text{g/m}^2$ , see legend) and for each of the four seasons over the Atlantic.

The anti-correlation between albedo and Ref is high (-0.77) for the annual data for the LWP range of  $25-50 \text{ g/m}^2$  only. The anti-correlation was lower (-0.33) for the LWP range of  $0-25 \text{ g/m}^2$  and negligible for  $LWP > 50 \text{ g/m}^2$ . Peng et al. (2002) showed that the effective radius is positively correlated with cloud albedo for polluted clouds caused by the absence of drizzle size drops. Conversely, effective radius is negatively correlated with cloud albedo for clean clouds. To explain our findings, further analysis should be performed including AOD as a measure of a dust content. Seasonal differences in pixel-by-pixel albedo-to-Ref relationship for different LWP ranges (Fig. 2.5) are not significant.

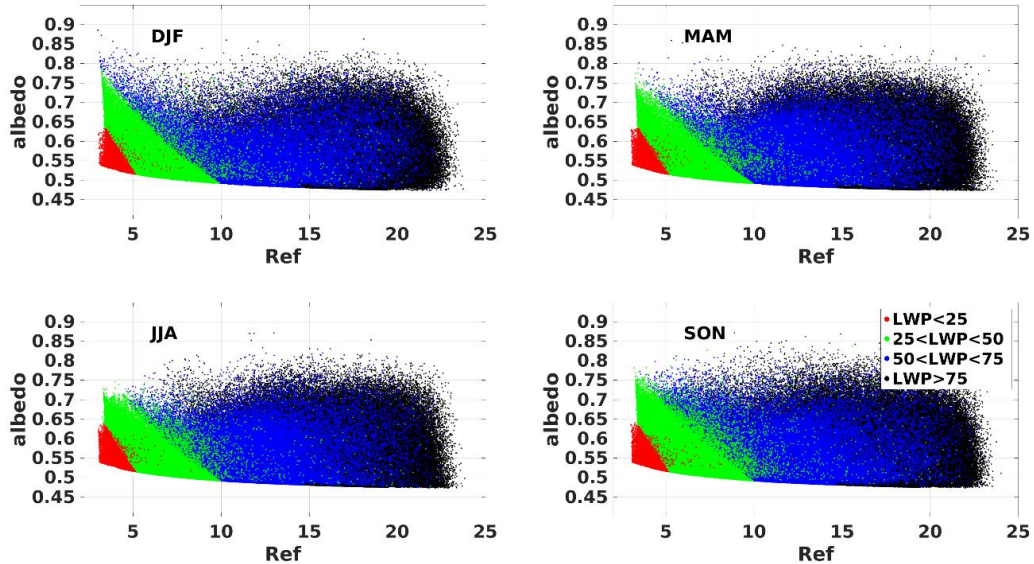


**Figure 2.5:** Scatterplots of albedo vs Ref for each pixel different LWP ranges ( $\text{g}/\text{m}^2$ , see legend) and for each of the four seasons over the Atlantic.

Even though seasonal differences in pixel-by-pixel albedo-to-COT and albedo-to-Ref relationships for different LWP ranges are not significant for the Atlantic area, the shape of the distributions is different from those for the other areas (Fig. 1S and 2S, supplement, not discussed here). Note the lower number of measurements over Europe in winter.

## 2.4 Discussion

The analysis of the monthly averaged aerosol and cloud properties, presented for year 2008, reveals the difference between the regions of interest. Overall, the correlation between AOD and cloud fraction increases for those regions with higher aerosol concentrations (as indicated by AOD which is used here as a proxy). Over the Atlantic, where dust and sea spray aerosols are dominating, the correlation between AOD and Ref and LWP has been analyzed, but a clear picture in terms of correlations has not been found. A more detailed analysis is required. More years are needed to consider year-to-year changes in meteorological conditions (e.g., monsoon intensity) in the same areas.

Uncertainties in the current study occur (but are not estimated) and are related to several reasons. Among them are the misclassification of aerosols as clouds cases of heavy aerosol loading (e.g., dust, biomass burning episodes or strong anthropogenic pollution – haze over Beijing). In the ADV test version, we performed a second run for AOD for the pixels, which are firstly classified as clouds, but COT for those pixels is low (<3). Those results are not shown here and will be further analyzed. The other reason, which may bias the statistical slopes, is that even when aerosol and cloud layers are detected, they may not be mixed (Costantino and Breon, 2010). For disconnected layers, an effect of aerosol particles on the cloud properties cannot be expected. However, accounting for this effect significantly improved the correlations (Liu et al., 2017).

## 2.5 Data availability

The database of L2 ( $0.1^\circ$  resolution, NetCDF format) aerosol and cloud AATSR daily data for 2008 for the regions mentioned above is available at FMI.

### 3 Analysis of ice formation efficiency based on Cloudnet observations (TROPOS, MPI-M, CUT)

Sections 3 and 4 deal with profiling of aerosol, cloud, and meteorological parameters by means of active ground-based remote sensing and UAVs. We begin with Cloudnet (lidar/radar) results.

The following data evaluation is based on the method published in Bühl et al. (2016). The efficiency of ice formation is analyzed by selecting mixed-phase cloud layers from the Cloudnet dataset. For each layer cloud top temperature (CTT) and the ice water content (IWC), particle fall velocity ( $v$ ) and linear depolarization ratio (LDR) are measured directly below cloud base. In this way, the flux of ice water mass from the cloud layer is determined which is proportional to the rate of ice formation in the mixed-phase cloud layer.

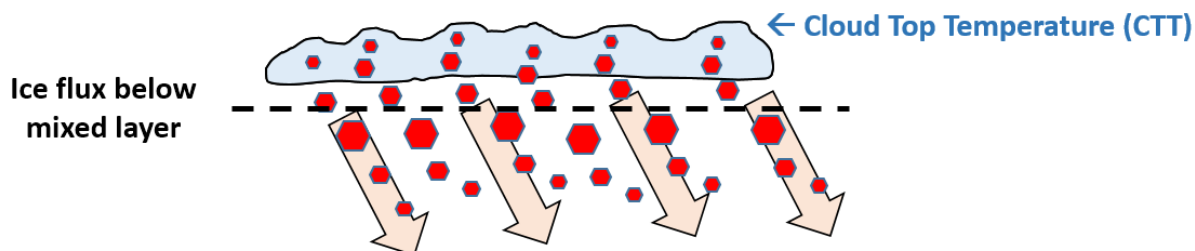


**Figure 3.1:** Illustration of the evaluation principle. The dashed line indicates the height level for which microphysical properties (IWC,  $v$  and LDR) of the ice particles falling from a cloud layer are evaluated.

#### 3.1 The new Barbados station integrated in the Cloudnet infrastructure

A preliminary Cloudnet dataset for the Barbados station was compiled during the early stages of the BACCHUS project. It contained combined ceilometer and cloud radar measurements of parts of the year 2013. A new Cloudnet dataset spanning the years 2013 to 2017 has been compiled in a cooperative project between MPI-M and TROPOS during the last 12 months. Figure 3.2 shows the measurements of IWC produced by mixed-phase cloud layers for different temperatures. It is visible that the mean values of IWC averaged over a 2.5 K interval are similar over Barbados and Leipzig for  $CTT < -10^\circ\text{C}$ . At Barbados, a low number of LDR values is obtained which is probably due to the larger height of the mixed-phase cloud layers over Barbados and the correspondingly lower SNR. LDR signatures around  $-5$  and  $-15^\circ\text{C}$  are similar between Leipzig and Barbados and are a clear sign that the dataset is of high quality. At  $-5^\circ\text{C}$ , long needle-like ice crystals or hollow crystals are expected. Both crystal types are non-spherical and produce high LDR values of around  $-15\text{dB}$ . At  $-15^\circ\text{C}$  stellar or plate-like ice crystals prevail, showing LDR values around  $-24\text{dB}$ . Figure 3.3 shows why the Barbados Cloudnet station is well suited for this kind of ice formation studies. The constant environmental conditions at Barbados show a predictable relation between temperature and height. Hence, cloud radar sensitivity is constant for all temperature intervals of CTT, eliminating seasonal and SNR biases.

Figure 3.4 shows ice formation in mixed-phase clouds over European Cloudnet stations and Barbados. The method for data evaluation is general and can be applied to all other available Cloudnet datasets in future. The flux of freshly formed ice from the mixed-phase cloud layers is observed to increase by at least one order of magnitude between  $-10$  and  $-30^\circ\text{C}$ . It is visible from Fig. 3.4 that the process of ice formation seems to be surprisingly uniform for all Cloudnet stations in Europe. Differences in the spread or shift of the ice flux are mainly within the instrumental and methodological uncertainties.

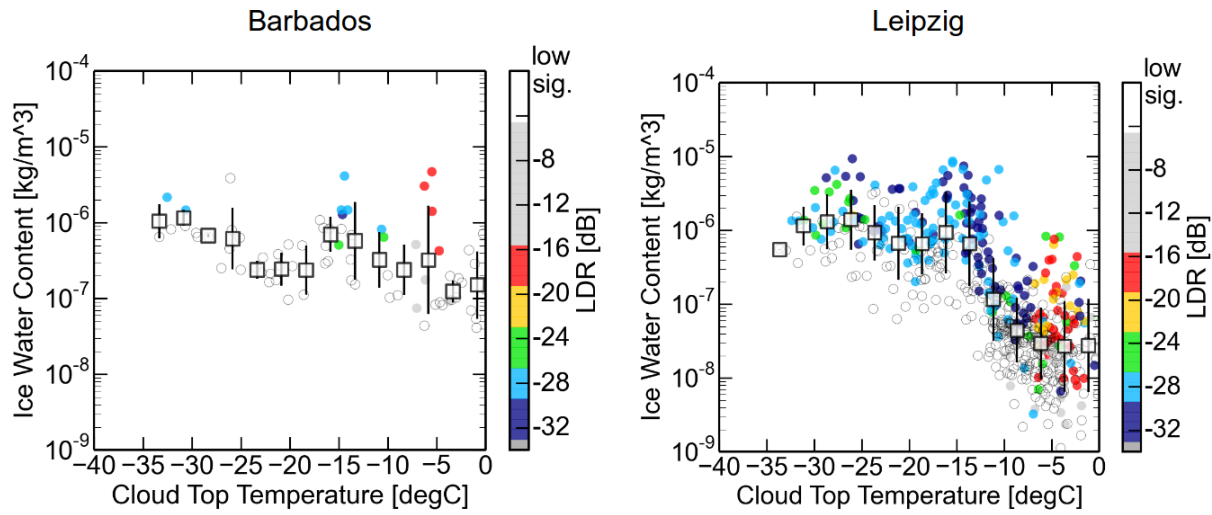


**Figure 3.2:** Comparison of ice water content (IWC at cloud base) measured at Barbados (left) and Leipzig (right). Squares and bars show mean values and standard deviations for 2.5 K temperature intervals.

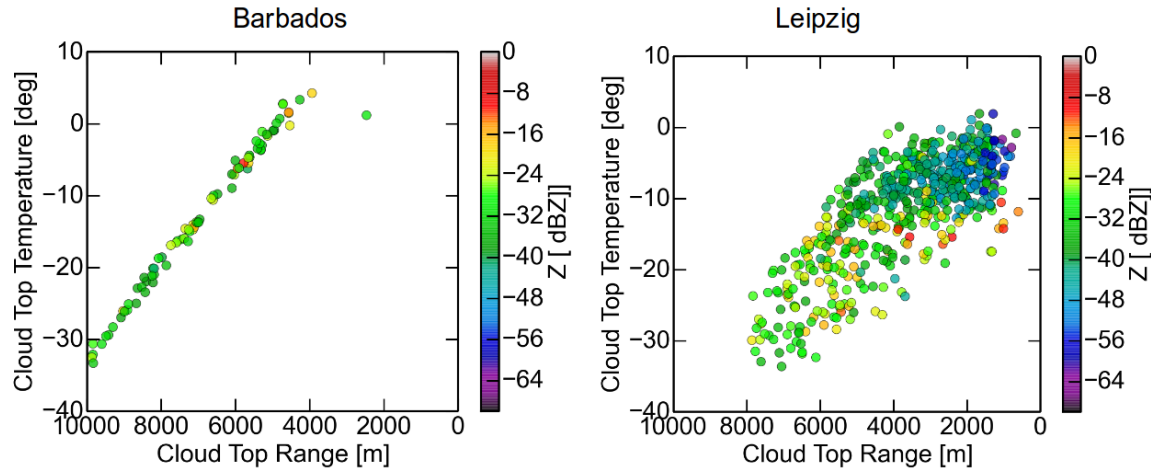


**Figure 3.3:** Relation of cloud top temperature (CTT) and cloud top height (CTH) for Barbados (left) and Leipzig (right) for all clouds under study.

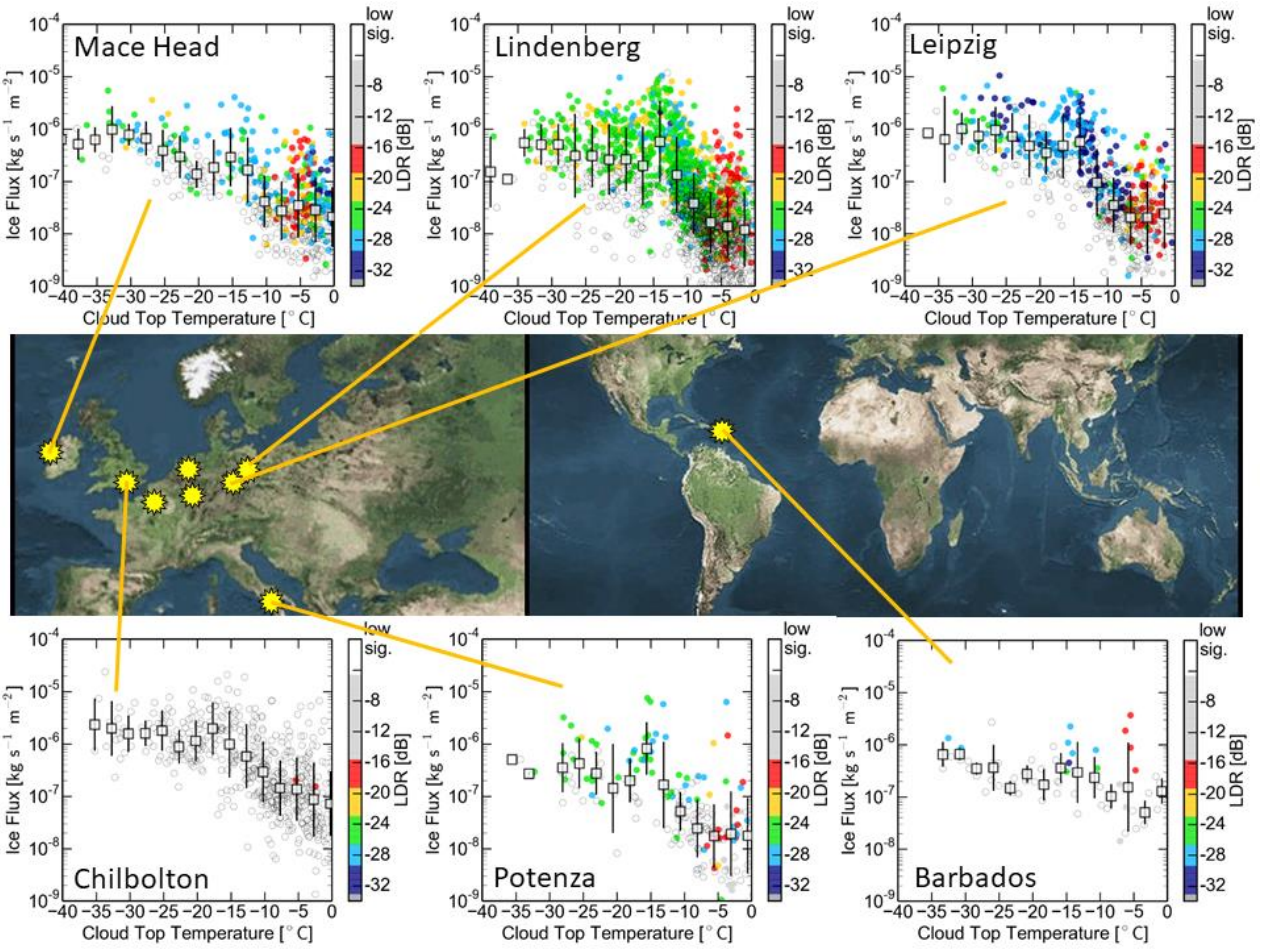


**Figure 3.4:** Compilation of ice formation efficiency in mixed-phase cloud layers of Earth's northern hemisphere. Empty squares indicate mean values for each 2.5 K interval.

### 3.2 Seasonally resolved statistics on ice fluxes

The long-term Cloudnet dataset of Lindenberg (12 years) allows us to contrast ice formation as function of cloud top temperature in different seasons. This differentiation may permit the study of a potential impact of biological and biogenic particles on ice formation. Figure 3.5 shows the ice flux out of mixed-phase cloud layers for the different seasons. The ice flux values are similar for the temperature range from -10 to -40°C. However, for the temperature range from 0 to -10°C, the lowest ice flux values are found in winter, and a factor of 2-3 higher values in summer and autumn (and probably in late spring, May). We may conclude that stronger convective processes in the summer half year transport more boundary-layer aerosol into the free troposphere (including biogenic particles). Also long-range transport of aerosols may favor ice formation because more dust outbreaks from Africa towards higher northern latitudes take place in the summer half year. Forest fire smoke from southern Europe and North America reach central Europe in summer. In winter, the free troposphere mainly contains aged background aerosol and the aerosol levels are reduced compared to the summer months.

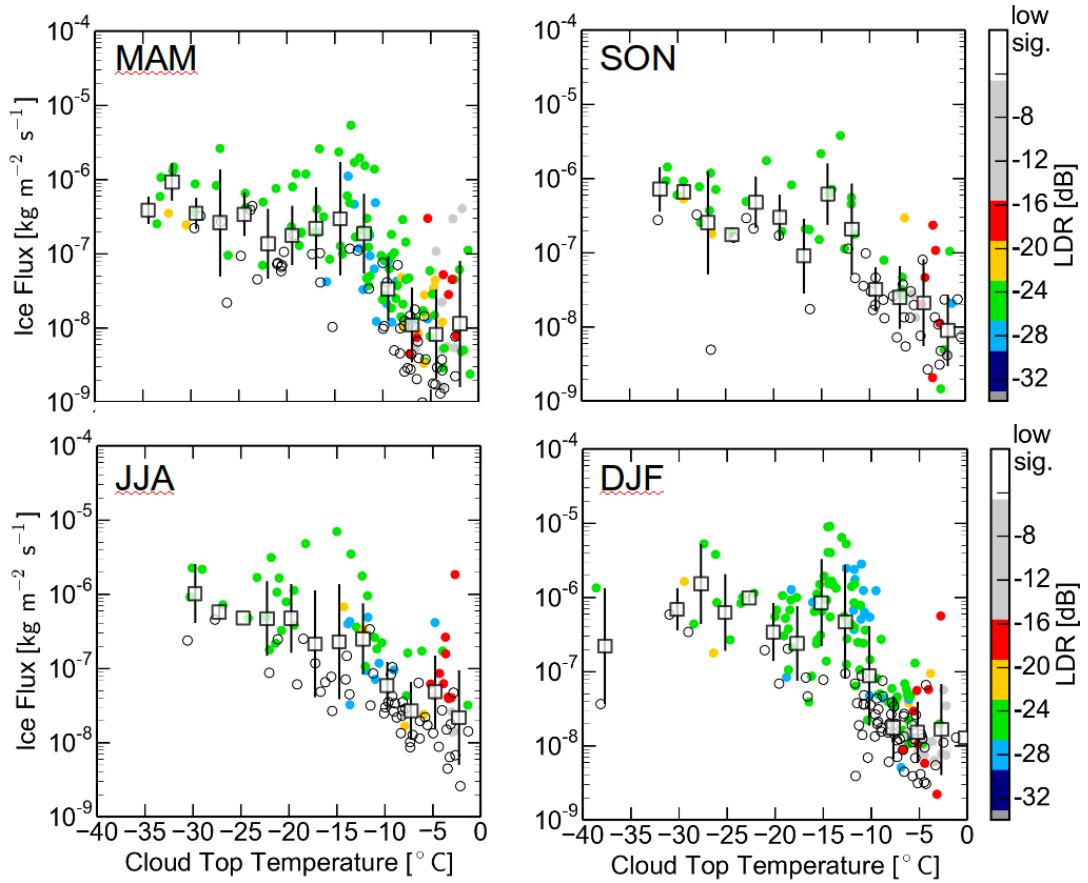


**Figure 3.5:** Ice flux observed directly below mixed-phase cloud layers at Lindenberg, Germany, in spring (MAM), summer (JJA), autumn (SON), and winter (DJF).

As a voluntary contribution of TROPOS to the BACCHUS project, the Leipzig Cloudnet station (Figure 3.6) was moved to the eastern Mediterranean in October 2016 to study cloud formation in the highly polluted and dust-rich Middle East region. The continuous observations at Limassol (CUT organized the field site and presently takes care of the measurements) in the framework of CyCARE (Cyprus Cloud Aerosol and Rain Experiment) will last until April 2018, and thus will cover two full rain seasons (November to March). Focus is on the impact of meteorological and aerosol conditions on the evolution of the ice phase in mixed-phase clouds in the EMME (Eastern Mediterranean/Middle East) region as well as the link to the formation of precipitation.

All Cloudnet observational products are stored in the Cloudnet data base which is part of the ACTRIS data base.



**Figure 3.6:** Overview of the LACROS facility at CUT premises, Limassol, Cyprus (Limassol Cloudnet station). The lidar container is equipped with a multi-wavelength aerosol polarization/Raman lidar PollyXT, a wind Doppler lidar, and radiation station (deployed in the summer of 2017 on the roof of the lidar container, the picture is from autumn 2016). The second LACROS container is equipped with a 35 GHz cloud radar (on the roof of the container, right), microwave radiometer (top, left), ceilometer (between the two containers), and a disdrometer (above the microwave radiometer for raindrop size distribution observations). The field site will be operated until April 2018 so that 18 months of continuous observations of aerosols, clouds, precipitation, and vertical winds will be available for studies of aerosol-cloud-dynamics relationships in the Eastern Mediterranean/Middle East region.

#### 4 Aerosol-cloud-radiation relationship observed with unmanned aerial vehicles (CNRS-GAME)

One of the BACCHUS goals is the quantification of key processes related to aerosol-cloud interactions and feedback effects by combining in-situ measurements with numerical modelling in climatically contrasting environments. The contributions from the Centre National de Recherches Météorologiques (CNRM/CNRS-GAME) focus on using unmanned aerial vehicles (UAVs), ground-based observations, and satellites to conduct studies on aerosol-cloud interactions. Two PhD students have been involved with this project (K. Sanchez; Univ. California San Diego, and R. Calmer; National Polytechnic Institute of Toulouse). Sanchez and Calmer have both submitted publications on their work.

Sanchez et al. (2017) presents top-down and bottom-up aerosol-cloud-radiative flux closures to better understand key processes affecting aerosol-cloud-radiative interactions. Instrument platforms included ground-based, UAVs, and satellite measurements of aerosols, clouds and meteorological variables. Aerosol-cloud parcel simulations are compared to airborne measurements of cloud extinction and show that entrainment processes significantly affect observed cloud microphysical properties (Fig. 4.1; adapted from Figure 8 in Sanchez et al., 2017). Excluding these entrainment processes in cloud models leads to overestimating the effective radiative forcing related to aerosol-cloud interactions between 10 and 50 W m<sup>-2</sup>. As expected, an overestimation of cloud radiative fluxes also occurs when using ground-based in situ observations (with much higher aerosol concentrations than at cloud base) in a de-coupled boundary layer; hence, there is a need to accurately represent CCN spectra near cloud base. Satellite-derived cloud droplet number concentrations were within 30% of entrainment-corrected simulated values. Sanchez et al. (2017) demonstrates the need for vertically probing the atmosphere to account for de-coupled layers and cloud-entrainment to accurately represent cloud radiative fluxes.

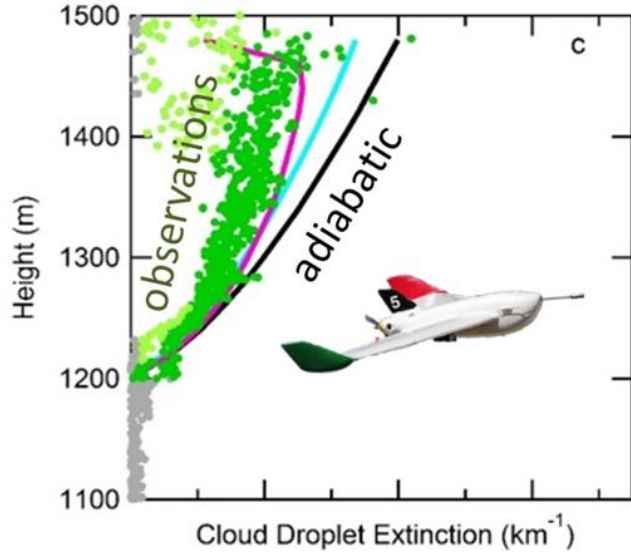


**Figure 4.1:** Vertical profiles of measured and simulated cloud extinction coefficient from UAV flights (adapted from Sanchez et al., 2017). In situ measurements are classified into cloud, cloud-transition and cloud-free observations. The differences between UAV-observed (green symbols) and simulated cloud extinction coefficients (black line for adiabatic; magenta, cyan lines represent parameterizations that include entrainment) is highlighted.

Calmer et al. (2017) focuses on the development and deployment of a multi-hole probe for the measurement of 3D winds (particularly, updraft) on UAVs, as vertical wind velocity at cloud base is a key parameter for assessing aerosol-cloud interactions. The 5-hole probe is calibrated and validated on a multi-axis platform in a wind tunnel. The 3D wind vectors from the UAV showed good agreement with results from a sonic anemometer on a 60 m.agl meteorological tower at P2OA, Lannemezan, France. Three case studies from a BACCHUS field campaign (at the Mace Head Atmospheric Research Station, Ireland) validated UAV vertical wind velocities in clouds compared to cloud radar observations. Vertical wind velocity distributions were classified according to the flight periods (clear sky or cloud), emphasizing the impact of meteorological processes and the state of the atmosphere on the clouds. For the first case study, a stratocumulus deck covered the sky and light precipitation was observed. Cloud radar vertical wind velocity distribution was negatively biased and cloud base was not distinctly visible due to falling droplets. The wind-UAV provided a centered vertical wind distribution near cloud base, which was similar to cloud radar observations at cloud-top (in the non-precipitating region of the cloud).

The second case study (Fig. 4.2 and 4.3; adapted from Figure 13 and 15 in Calmer et al., 2017, respectively) displayed different meteorological conditions during the flight, which were well distinguished by the wind-UAV, including differences between a developing field of broken clouds, a small convective cloud and clear sky. In the third case study, similar vertical wind distributions were observed near cloud base by the UAV and the cloud radar in fair weather cumulus cloud systems above land and ocean. The distinct meteorological conditions which were encountered for each of the case studies validated UAV results compared to cloud radar and highlighted the ability of the UAV platform to differentiate cloud systems based on vertical wind measurements for different conditions. Vertical wind velocities near cloud base measured in this study have been implemented in air parcel models to conduct aerosol-cloud closure studies with ground-based measurements, UAVs, and satellite observations (Sanchez et al., 2017). A second aerosol-cloud closure case study from a field experiment in Cyprus is currently underway; preliminary results confirm the importance of including entrainment for estimating stratocumulus cloud optical properties even at relatively high aerosol concentrations and stronger updraft velocities.

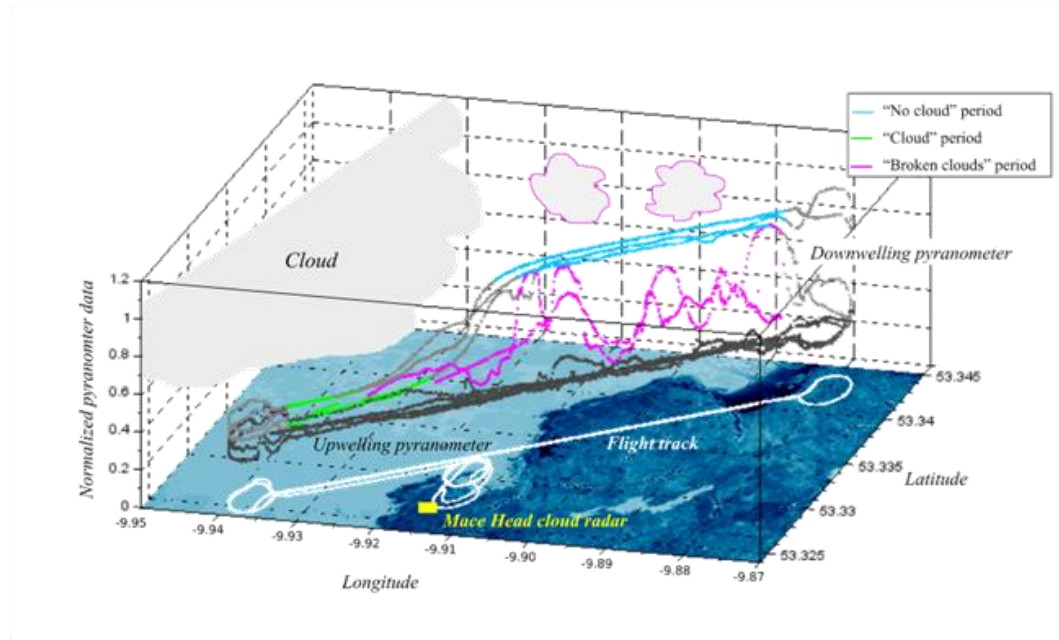


**Figure 4.2:** Flight tracks for the case study of a convective cloud with changing meteorological conditions. Downwelling and upwelling pyranometer data are color-coded based on the three flight periods (“cloud”, “no cloud” and “broken clouds”). The developing field of broken clouds (magenta contour clouds) appeared during the last two legs. The cloud radar (yellow square) operated at the Mace Head research station.

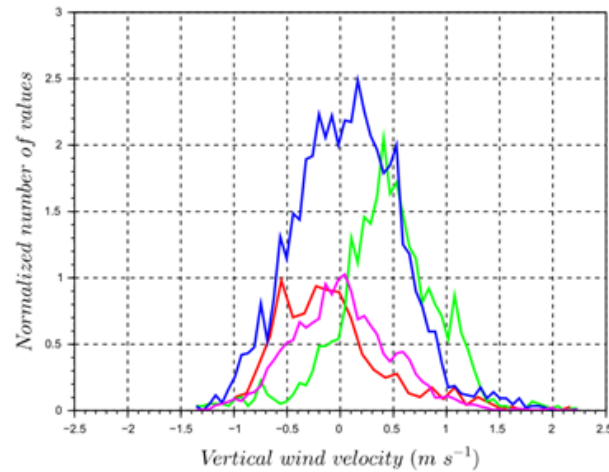


**Figure 4.3** Comparison of vertical wind velocity distributions for UAV (green during cloud periods in Fig. 4.2 blue during cloud free periods, magenta during periods with broken cloud fields) and cloud radar (red). Cloud radar data are available for the broken cloud period only.

## **5 Establishment of an ice nucleating particle database (INDB, ETHZ)**

The BACCHUS project aims to quantify the influence of anthropogenic aerosols on cloud properties and to advance the understanding of key cloud-aerosol interactions and feedback mechanisms. As a part of the strategy for INP, the creation of a data base of field observations is included. For various atmospheric species a large data facility exists – ACTRIS. For INP no easy-to-access store of data exists. Here we report on an INP data base created as part of the BACCHUS project.

Before a detailed description of the new INP data base is given, we briefly summarize the overall BACCHUS concept regarding CCN and INP data bases. One of the central tasks of BACCHUS is to perform new INP and new CCN observations and to re-analyze existing CCN data sets. The CCN measurements are then provided to the ACTRIS data network and hence handled according to the ACTRIS data protocol. This ensures best possible dissemination of the long-term data sets to the research community. As such the CCN data are formatted to match the ACTRIS requirements. The BACCHUS CCN data are integrated into the ACTRIS framework which is then transferred into the GASSP (Global Aerosol Synthesis and Science Project) project (Reddington et al., 2017). To provide easy access to the GASSP partner institutions, the GASSP data base is hosted in the UK Centre for Environmental Data Archival (CEDA, <http://www.ceda.ac.uk/>) Jasmine facility (<http://www.jasmin.ac.uk/>). The current arrangement provides read access to scientists participating directly in GASSP, along with those who have accepted the GASSP Data Exchange Protocol (DEP). The ACTRIS data policy and data format descriptions are available online (<http://actris.nilu.no/Content/Documents/DataPolicy.pdf>; data format: [http://www.actris.net/portals/97/Publications/quality%20standards/aerosol%20insitu/WP3\\_D3.13\\_M24\\_CCNC\\_SOP\\_v130514.pdf](http://www.actris.net/portals/97/Publications/quality%20standards/aerosol%20insitu/WP3_D3.13_M24_CCNC_SOP_v130514.pdf)).

In contrast to the well-established and organized ACTRIS data network infrastructure including the CCN data base, an equivalent INP data base was not existing in the beginning of the BACCHUS project. During meetings at the start of BACCHUS, it was suggested that the BACCHUS INP database could utilize a design as realized for CCN in the case of the GASSP project (<http://gassp.org.uk/>).

The BACCHUS INP Database (INDB) is a tool for the ice nucleation community, not only to help inform observational campaign planning but also to facilitate the provision of data to modelling studies and comparison reviews.

The INDB is designed such that each dataset has two entries - the first which details all the general information of the dataset such as location, instrumentation and sampling conditions, and a second containing the data itself. This design allows for flexibility in the format and location of contributed data, as the search process only accesses the first of these two sections. Therefore, the actual data file can be in any format or even absent if storage in a 3rd party archive is prohibited by funding bodies. Of course, accepting data in any format would quickly make a large database impractical so datasets will ultimately be stored in NetCDF format. The flexibility in data format also allows the INDB to take a wide range of data types. The only requirements for data contribution are that the data relate to atmospheric INP concentration and/or chemical composition observations with a known location. In the future, the INDB could be opened up to include laboratory studies of INP and also field observations of ice residuals.

All contributed data are legally protected by a data protocol (see section 5.1), which protects the data providers ownership of all data including unpublished data. Accepting the protocol is a prerequisite to accessing the INDB; this protocol has been included into the BACCHUS Consortium Agreement and explicitly agreed to by all BACCHUS partners.

The BACCHUS INDB can be accessed through the following link: <http://www.bacchus-env.eu/in/index.php>. The database is designed so that users can contribute data and search for existing data. Database users are not be confined to BACCHUS scientists. To use the

INDB the user needs to enter (light blue, Fig. 5.1) their data requirements into the search page. Depending on the availability of data, they then either contact the contributor, or directly download the data. Contributor (purple, Fig. 5.1): provides campaign details to the search page for user searches, and either provides a file for direct download or responds directly to user data queries. Not all campaigns have data files. This feature is so that it allows the inclusion of campaigns before publication of data, quality control of data, or even before the campaign has occurred (not recommended).

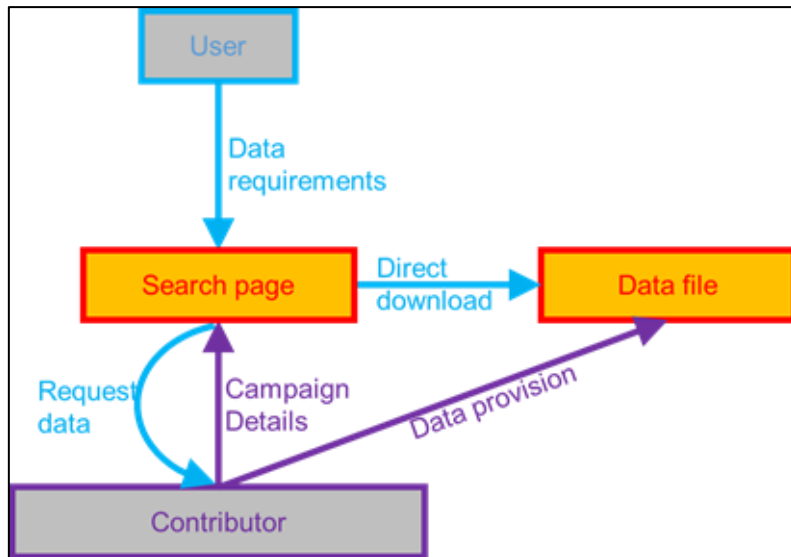


**Figure 5.1:** BACCHUS ice nucleation database structure.

To gain access to the INDB a completed hard copy of the data-protocol is needed (available on the database website [bacchus-env.eu/in/](http://bacchus-env.eu/in/)). Digital copies are not accepted. The signed protocol forms then needed to be mailed to the BACCHUS project office at ETHZ.

Currently the database contains 77 entries, of which 43 have files available for immediate download. The spatial distribution of these entries are shown in Fig. 5.2.

Based on Fig. 5.2, it is clear that USA and Europe are spatially well covered relative to Asia, Africa and South America. Arctic and Antarctic in addition have poor coverage of INP measurements, although through recent field campaigns (both ship, and aircraft based), new data will become available for these locations in the next few months. While the Southern Ocean appears to be well covered, it should be mentioned that the corresponding data coverage shown in Fig. 5.2 is based on single data points where as in the locations shown for Europe and USA encompass many campaigns and full campaigns over the course of weeks to months. Lastly, many sites that do have good coverage may be limited in the temperature range at which the INP concentrations are reported. Thus at some temperature, most areas shown have a poor coverage.

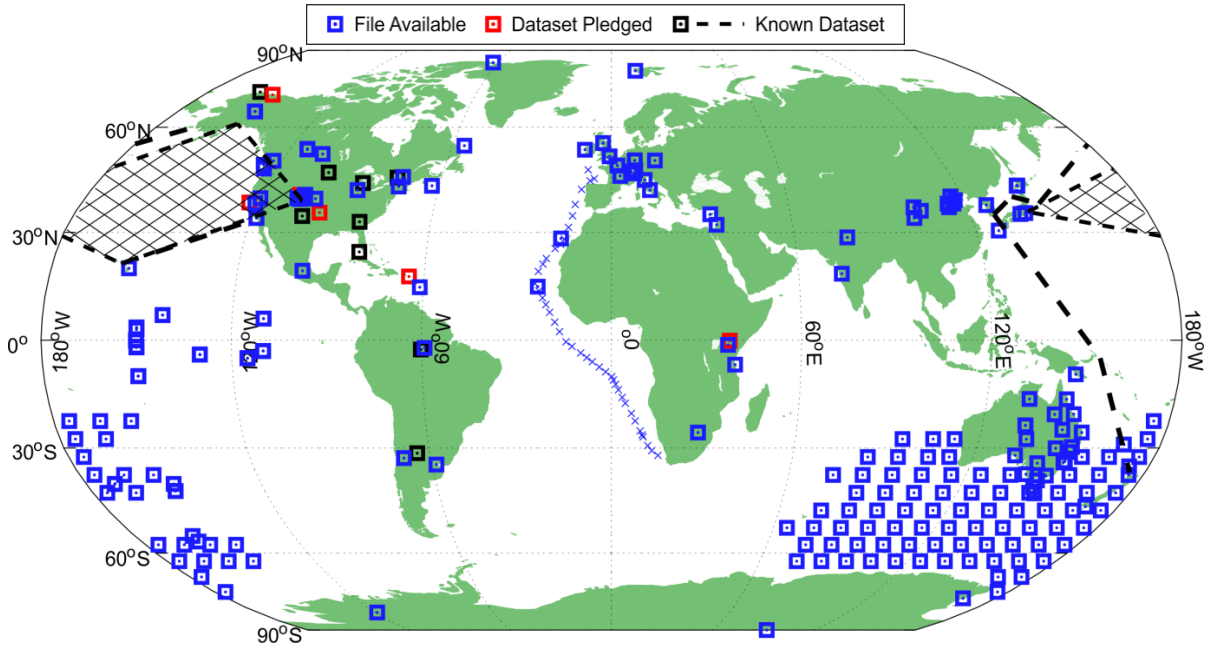


**Figure 5.2:** Searchable datasets in the INDB. BACCHUS Field sites include: Nicosia, Cyprus, Zurich (ZAMBIS campaign) and JFJ (Boose et al., 2016a; Lacher et al., 2017) in Switzerland, Mace Head, Ireland, Tenerife, Spain (Boose et al., 2016b), Martinique, Amazon, Brazil, Svalbard, Norway, Taunus Observatory, Germany and Bologna, Italy.

The range of temperature coverage for some exemplary locations is shown in Fig. 5.3. For example in the British Isles and Amazon, INP have been measured for a longer time period, but only at three discrete temperatures, whereas for a location like Cyprus a better temperature range of INP has been achieved within the framework of the BACCHUS project. Here it should be mentioned that the possibility to cover larger temperature ranges (235 to 273 K) requires the use of two different techniques, an online and offline measurement technique. Most offline techniques so far are able to report data for the first 25 degrees of supercooling, followed by online techniques, which become important to quantify INP in the temperature range 238 – 248 K. The use of two different techniques may present some limitations depending on what is desired. The offline techniques despite covering a large temperature range, are limited in temporal resolution to a time span typically of hours up to 24 hours (Cziczo et al., 2017). The online techniques are limited to colder temperature sampling because of sensitivity issues, but can report INP concentrations for a time resolution as high at 10-20 minutes (Cziczo et al., 2017).

What is also visible from the data in Fig. 5.3, is that much of the INP data is collected as part of intensive field campaigns. For example the sub-plot referring to Central Europe, shows a large variation of INP concentrations at a given temperature. This is indicative of longer (1-2 months) intensive field campaigns, sampling at a single or at most two temperatures. The limitation here is twofold, the number of online instruments that can be deployed is limited because of economic costs. But more importantly the lack of a completely automated online INP instrument also means man power limits sampling time and therefore temperature range. The advantage of the data collected thus far in the BACCHUS INDB, is that it can be used to decide where future campaigns should be held in order to fill in the gaps for spatial coverage.

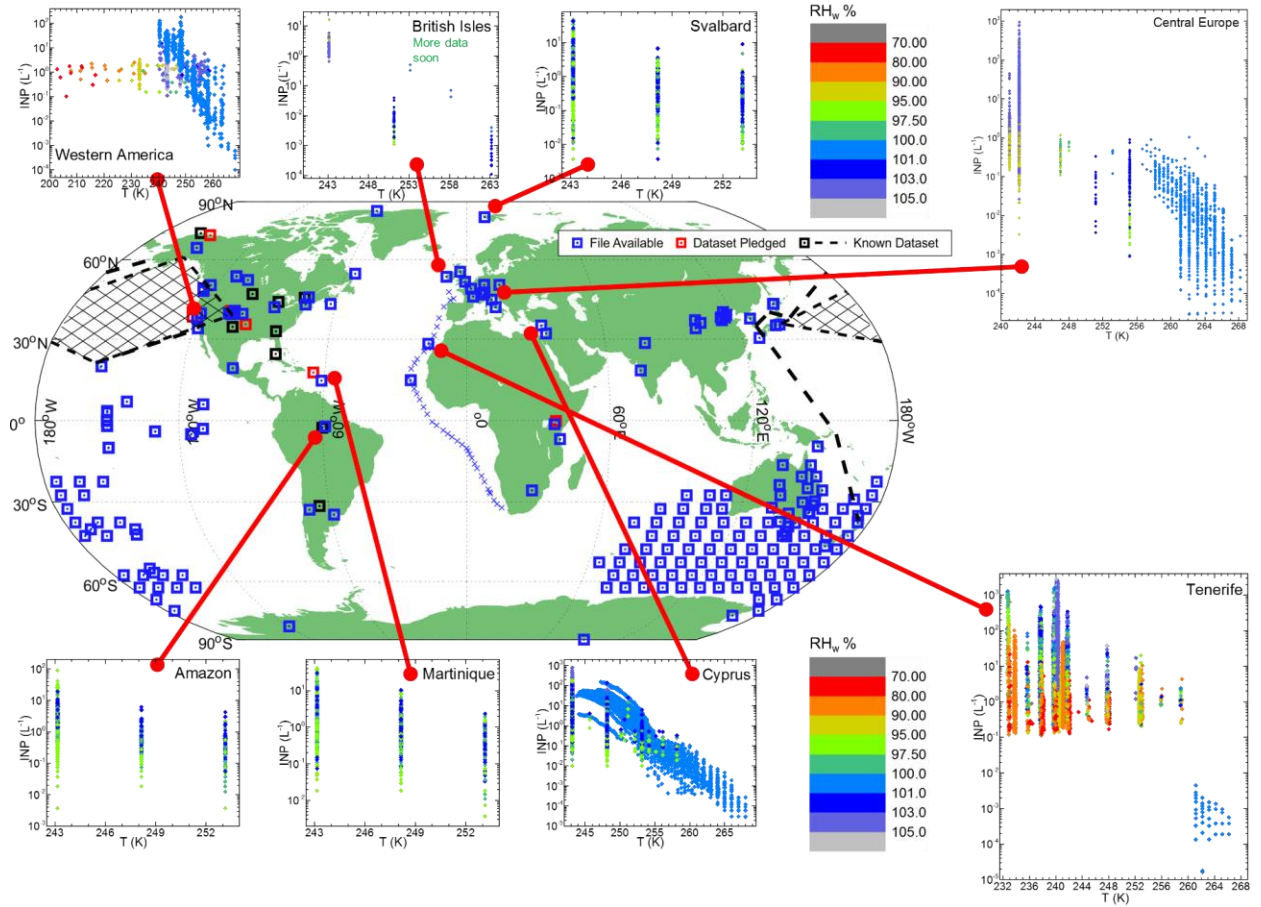


**Figure 5.3.** Geographic summary of INP concentration observations. The figures provide the INP concentrations with temperature of data **available in the database**. RH<sub>w</sub> provided by the symbol colours (all figures use the same colour scheme).

Other advantages of the INDB even at this stage of data population (many pledged data sets yet to come), includes visualizing the data to assess the impacts of various parameters. For example in Figure 5.4, we plot regardless of the location, the INP concentration as a function of the temperature and sampling relative humidity with respect to water (RH<sub>w</sub>) at which these INP concentrations are reported.

A general trend of high INP at high RH<sub>w</sub> and low temperature is visible. Preliminary fits to the data at high RH<sub>w</sub> are provided. Data at lower temperatures is predominantly from single particle continuous flow diffusion chambers, which tend to have a lower limit of ~0.1 INP L<sup>-1</sup> for sampling due to their limit of detection. Therefore estimating fits at low RH<sub>w</sub> (and low INP) was not possible. On average what is also visible is that some of the older parameterizations [e.g. Cooper, 1986] predict fairly well the average INP concentrations at least in the relevant temperature range as shown in Figure 5.4.

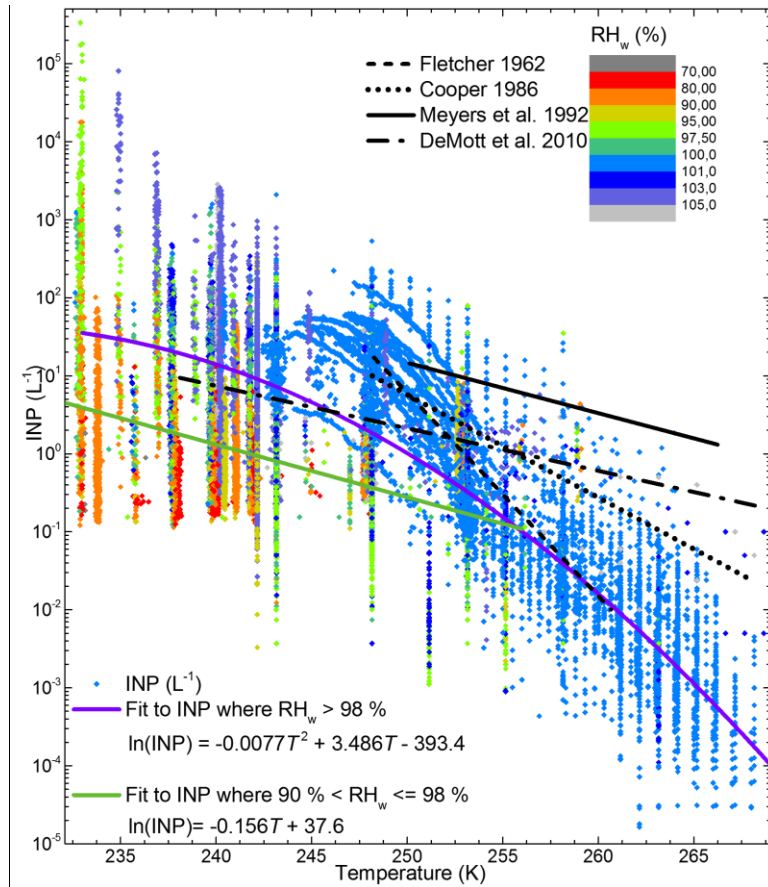


**Figure 5.4.** INP concentration vs temperature for all campaigns in the database; the symbol colour indicates the measurement RH<sub>w</sub>.

Similar to what is done in Figure 5.4, other parameters can be assessed against INP. For example, visualizing the INP as a function of altitude (Figure 5.5) or INP as a function of RH<sub>w</sub> at a fixed temperature (Figure 5.6). These visualizations are also useful in planning future measurement campaigns. For example, how to select the altitude for future field campaigns. From the data shown in Figure 5.5, at first glance it appears there is no specific advantage at conducting measurements at high altitude, since INP concentrations are not better constrained with altitude for the first 4 km. At higher altitudes it appears as though the concentrations are more confined. But one would have to question whether the temporal coverage is the same as the lower altitudes, and it is not. In which case would longer sampling times at the very high altitudes (above 4 km) also yield a large range of INP concentrations? In addition, the lower limit of 0.1 L<sup>-1</sup> also begs the question if in fact the values are more confined at high altitudes because of the instrument lower limit. Lastly, even though the ranges in INP concentrations for the mid-altitude data are quite large, one can clearly see that the maximum INP concentrations are achieved in the boundary layer measurements at ground level of up to 105 L<sup>-1</sup> which are not representative of INP number concentrations in the mid-troposphere based on current knowledge. Thus when examining why the range of INP concentrations can be so large at a given temperature spanning for example six orders of magnitude (see cyan data points at ~3600 m), one should keep in mind that the range of concentrations at a single location (e.g. the vertical lines of points) is due to measurement and meteorological conditions, location, the amount of influence from the local boundary layer and long range transport. These factors appear to be more important than the altitude of the measurements in determining the INP concentration.

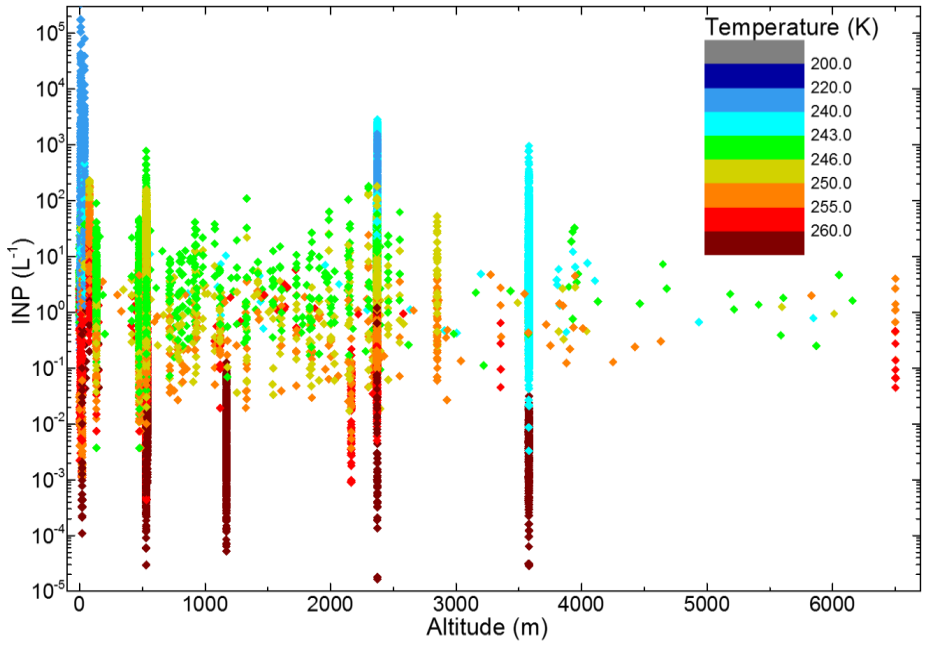


**Figure 5.5** INP trend with altitude. The vertical lines of measurements indicate surface/ground based campaigns whereas other data are from airborne campaigns.

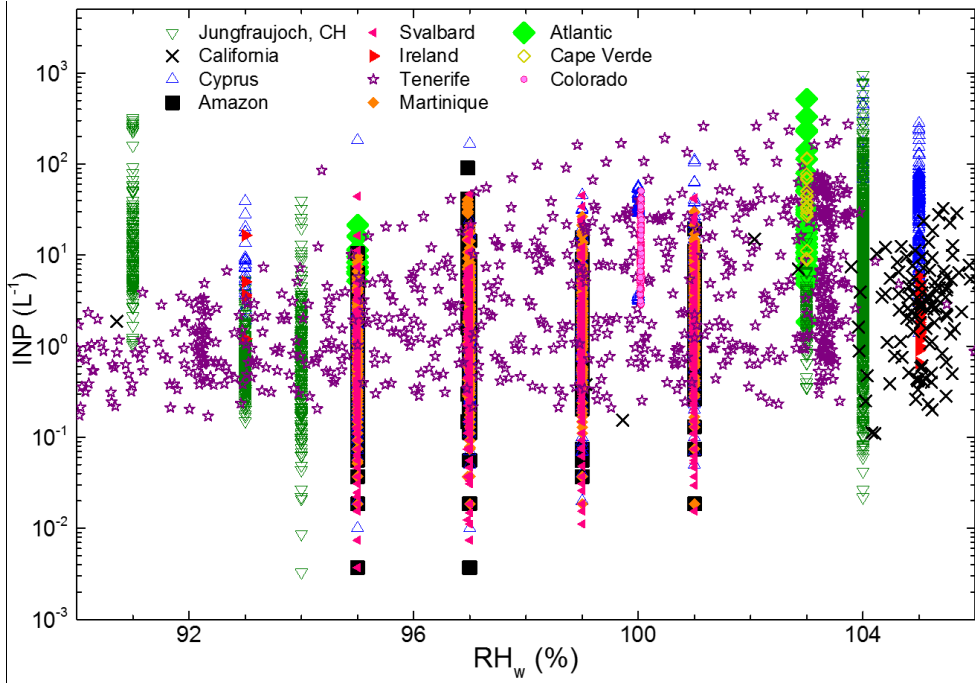


**Figure 5.6** INP concentration vs.  $RH_w$  at  $243 \pm 2$  K in different regions. Except for Jungfraujoch (~91 %) which on that occasion had strong influence from a dust source, all data from these locations seem to have a maximum value of  $\sim 20$  INP  $L^{-1}$  below  $\sim 96$  % and  $\sim 300$  INP  $L^{-1}$  above  $\sim 100$  %.

A future plan for the BACCHUS INDB in addition to continuing being available for contribution of data to modellers and accepting new datasets from pledged and future field campaigns is the assignment of a DOI (digital object identifier) for contributed data sets. This ensures all contributors and potential publication authors that the data sets are easily

identified for easy use, accessibility and future data management policy plans that are already being implemented by many research funding agencies.

## 5.1 INDB Data Protocol

At the end one should mention, that two BACCHUS Data Protocols (BACCHUS DP) were developed:

- (1) The BACCHUS Internal DP aims to uphold the rights of individual scientists while encouraging the rapid dissemination of the scientific results, by regulating data delivery, data exchange and storage, and the interaction between measuring participants. This protocol is additive to the BACCHUS Consortium Agreement (CA) signed July 4th, 2013, and no regulation in this protocol may contradict the rules set forth in the CA.
- (2) The BACCHUS INP Data Base Protocol for external users (final version 1, 10 February 2015, updated on 06 September 2016). One aim of BACCHUS is to create a database of global INP observations to facilitate the understanding of ice nucleation processes. The aims of the BACCHUS INP Database Protocol are (a) to define the acceptable use of data by external users; (b) to protect the data ownership of the contributing scientists; (c) recognize the contribution made by other scientists in terms of data processing (data synthesis, merging, etc); (d) define and regulate how the datasets will be managed and stored. This protocol may be superseded by existing data protocols of the data providers, which the users of the data will sign.

## References

- Andreae, M. O., et al: The Amazon Tall Tower Observatory (ATTO): overview of pilot measurements on ecosystem ecology, meteorology, trace gases, and aerosols, *Atmos. Chem. Phys.*, 15, 10723—10776, doi:10.5194/acp-15-10723-2015, 2015.
- Boose, Y., Z. A. Kanji, M. Kohn, B. Sierau, A. Zipori, I. Crawford, G. Lloyd, N. Bukowiecki, E. Herrmann, P. Kupiszewski, M. Steinbacher, and U. Lohmann: Ice Nucleating Particle Measurements at 241 K During Winter Months at 3580 M asl in the Swiss Alps, *Journal of the Atmospheric Sciences*, 73(5), 2203-2228, doi:10.1175/JAS-D-15-0236.1, 2016a.
- Boose, Y., B. Sierau, M. I. García, S. Rodríguez, A. Alastuey, C. Linke, M. Schnaiter, P. Kupiszewski, Z. A. Kanji, and U. Lohmann: Ice Nucleating Particles in the Saharan Air Layer, *Atmospheric Chemistry and Physics*, 16(14), 9067-9087, doi:10.5194/acp-16-9067-2016, 2016b.
- Bühl, J., Seifert, P., Myagkov, A. & Ansmann, A., Measuring ice- and liquid-water properties in mixed-phase cloud layers at the Leipzig Cloudnet station. *Atmospheric Chemistry and Physics*, 16, 10609-10620, 2016.
- Calmer, R., Roberts, G., Preissler, J., Derrien, S., and O'Dowd, C.: 3D Wind Vector Measurements using a 5-hole Probe with Remotely Piloted Aircraft, *Atmos. Meas. Tech. Discuss.*, <https://doi.org/10.5194/amt-2017-233>, in review, 2017.
- Cooper, W. A.: Ice Initiation in Natural Clouds, *Meteorological Monographs*, 43, 29-32, doi:10.1175/0065-9401-21.43.29, 1986.
- Costantino, L., and F.-M. Bréon: Analysis of aerosol-cloud interaction from multi-sensor satellite observations, *Geophys. Res. Lett.*, 37, L11801, doi:10.1029/2009GL041828, 2010.

- Cziczo, D. J., L. Ladino, Y. Boose, Z. A. Kanji, P. Kupiszewski, S. Lance, S. Mertes, and H. Wex: Measurements of Ice Nucleating Particles and Ice Residuals, Meteorological Monographs, 58, 8.1-8.13, doi:10.1175/AMSMONOGRAPH-D-16-0008.1, 2017.
- DeMott, P. J., A. J. Prenni, X. Liu, S. M. Kreidenweis, M. D. Petters, C. H. Twohy, M. S. Richardson, T. Eidhammer, and D. C. Rogers: Predicting Global Atmospheric Ice Nuclei Distributions and Their Impacts on Climate, Proceedings of the National Academy of Sciences of the United States of America, 107(25), 11217-11222, doi:10.1073/pnas.0910818107, 2010.
- Guo, Z., and T. J. Zhou: Seasonal variation and physical properties of the cloud system over southeastern China derived from CloudSat products. *Adv. Atmos. Sci.*, 32(5), 659–670, 2015.
- Hashimshoni, E.: Retrieval of CCN(S) in pristine environments as analogue to the pre-industrial era, master thesis, The Hebrew University of Jerusalem, Israel, October 2017.
- Jiang, Y. Q., X. H. Liu, X. Q. Yang, et al.: A numerical study of the effect of different aerosol types on East Asian summer clouds and precipitation. *Atmos. Environ.*, 70, 51–63, 2013.
- Kokhanovsky, A. A., V. V. Rozanov, E. P. Zege, H. Bovensmann, and J. P. Burrows, A semianalytical cloud retrieval algorithm using backscattered radiation in 0.4–2.4  $\mu\text{m}$  spectral region, *J. Geophys. Res.*, 108, 4008, doi:10.1029/2001JD001543, 2003.
- Kolmonen, P., Sogacheva, L., Virtanen, T., de Leeuw, G., and Kulmala, M, The ADV/ASV AATSR aerosol v2.30 retrieval algorithm: current status and presentation of a full-mission AOD data set. *Int. J. of Digital Earth*, p.1-17, DOI: 10.1080/17538947.2015.1111450, 2016.
- Koren, I., Y. J. Kaufman, L. A. Remer, and J. V. Martins: Measurement of the effect of Amazon smoke on inhibition of cloud formation, *Science*, 303, 1342–1345, 2004.
- Koren, I., L. A. Remer, Y. J. Kaufman, Y. Rudich, and J. V. Martins, On the twilight zone between clouds and aerosols, *Geophys. Res. Lett.*, 34, L08805, 2007.
- Lacher, L., U. Lohmann, Y. Boose, A. Zipori, E. Hermann, N. Bukowiecki, M. Steinbacher, and Z. A. Kanji: The Horizontal Ice Nucleation Chamber HINC: INP Measurements at Conditions Relevant for Mixed-Phase Clouds at the High Altitude Research Station Jungfraujoch, *Atmospheric Chemistry and Physics Discussions*, in review, doi:10.5194/acp-2017-474, 2017.
- Laken, B. A., Parviainen, H., Pallé, E. and Shahbaz, T., Saharan mineral dust outbreaks observed over the North Atlantic island of La Palma in summertime between 1984 and 2012. *Q.J.R. Meteorol. Soc.*, 140: 1058–1068. doi:10.1002/qj.2170, 2014.
- Li, Z., et al., Aerosol and monsoon climate interactions over Asia, *Rev. Geophys.*, 54, 866–929, doi:10.1002/2015RG000500, 2016.
- Li, W. H., R. Fu, and R. E. Dickinson, Rainfall and its seasonality over the Amazon in the 21st century as assessed by the coupled models for the IPCC AR4, *J. Geophys. Res.*, 111, D02111, doi:10.1029/2005JD006355, 2006.
- Liu, Y., de Leeuw, G., Kerminen, V.-M., Zhang, J., Zhou, P., Nie, W., Qi, X., Hong, J., Wang, Y., Ding, A., Guo, H., Krüger, O., Kulmala, M., and Petäjä, T.: Analysis of aerosol effects on warm clouds over the Yangtze River Delta from multi-sensor satellite observations, *Atmos. Chem. Phys.*, 17, 5623-5641, <https://doi.org/10.5194/acp-17-5623-2017>, 2017.

- Luo, M., Leung, Y., Graf, H., Herzog, M., & Zhang, W., Interannual variability of the onset of the South China Sea summer monsoon. International Journal of Climatology, 36 550-562. <https://doi.org/10.1002/joc.4364>, 2015.
- Martins, G., von Randow, C., Sampaio, G., and Dolman, A. J.: Precipitation in the Amazon and its relationship with moisture transport and tropical Pacific and Atlantic SST from the CMIP5 simulation, Hydrol. Earth Syst. Sci. Discuss., <https://doi.org/10.5194/hessd-12-671-2015>, 2015.
- Meyers, M. P., P. J. Demott, and W. R. Cotton: New Primary Ice-Nucleation Parameterizations in an Explicit Cloud Model, Journal of Applied Meteorology, 31(7), 708-721, doi:10.1175/1520-0450(1992)031<0708:npinpi>2.0.co;2, 1992.
- Patil N., Dave P., and Venkataraman, C.: Contrasting influences of aerosols on cloud properties during deficient and abundant monsoon years. Scientific Reports. 2017;7:44996. doi:10.1038/srep44996, 2017.
- Peng, Y., U. Lohmann, R. Leaitch, C. Banic, and M. Couture, The cloud albedo–cloud droplet effective radius relationship for clean and polluted clouds from RACE and FIRE.ACE, J. Geophys. Res., 107(D11), 4106, doi:10.1029/2000JD000281, 2002.
- Reddington, C., et al, The global aerosol synthesis and science project (GASSP): Measurements and modeling to reduce uncertainty, B. Amer. Meteorol. Soc., 98, pp.1857-1877. doi: 10.1175/BAMS-D-15-00317.1, 2017.
- Rosenfeld, D.: Suppression of Rain and Snow by Urban and Industrial Air Pollution. Science 287: 1793-1796, 2000.
- Rosenfeld, D., et al., Satellite retrieval of cloud condensation nuclei concentrations by using clouds as CCN chambers. Proceedings of the National Academy of Sciences, 113, 5828-5834, 2016.
- Sanchez, K. J., Roberts, G. C., Calmer, R., Nicoll, K., Hashimshoni, E., Rosenfeld, D., Ovadnevaite, J., Preissler, J., Ceburnis, D., O'Dowd, C., and Russell, L. M.: Top-down and bottom-up aerosol–cloud closure: towards understanding sources of uncertainty in deriving cloud shortwave radiative flux, Atmos. Chem. Phys., 17, 9797-9814, <https://doi.org/10.5194/acp-17-9797-2017>, 2017.
- Takemura, T., Y. J. Kaufman, L. A. Remer, and T. Nakajima: Two competing pathways of aerosol effects on cloud and precipitation formation, Geophys. Res. Lett.,34, L04802,doi:10.1029/2006GL028349, 2007.
- Rosenfeld, D. Suppression of Rain and Snow by Urban and Industrial Air Pollution. Science 287: 1793-1796, 2000.
- Sogacheva, L., Kolmonen, P., Virtanen, T. H., Rodriguez, E., Sundström, A.-M., and de Leeuw, G.: Determination of land surface reflectance using the AATSR dual-view capability, Atmos. Meas. Tech., 8, 891-906, doi:10.5194/amt-8-891-2015, 2015.
- Sogacheva, L., Kolmonen, P., Virtanen, T. H., Rodriguez, E., Saponaro, G., and de Leeuw, G.: Post-processing to remove residual clouds from aerosol optical depth retrieved using the Advanced Along Track Scanning Radiometer, Atmos. Meas. Tech., 10, 491-505, doi:10.5194/amt-10-491-2017, 2017.
- Tang, J., Wang, P., Mickley, L. J., Xia, X., Liao, H., Yue, X., Sun, L., Xia, J., Positive relationship between liquid cloud droplet effective radius and aerosol optical depth over Eastern China from satellite data. Atm. Env., 84, 244-253, 2014.
- Twomey, S.: Influence of pollution on the short-wave albedo of clouds. J. Atmos. Sci, 34, 1149-1152, 1977.

- van der Does, M., Korte, L. F., Munday, C. I., Brummer, G.-J. A., and Stuut, J.-B. W.: Particle size traces modern Saharan dust transport and deposition across the equatorial North Atlantic, *Atmos. Chem. Phys.*, 16, 13697-13710, <https://doi.org/10.5194/acp-16-13697-2016>, 2016.
- Virtanen, T. H., Kolmonen, P., Rodríguez, E., Sogacheva, L., Sundström, A.-M., and de Leeuw, G.: Ash plume top height estimation using AATSR, *Atmos. Meas. Tech.*, 7, 2437-2456, doi:10.5194/amt-7-2437-2014, 2014.
- Westervelt, D. M., Moore, R. H., Nenes, A., and Adams, P. J.: Effect of primary organic sea spray emissions on cloud condensation nuclei concentrations, *Atmos. Chem. Phys.*, 12, 89-101, <https://doi.org/10.5194/acp-12-89-2012>, 2012.

### **Changes with respect to the DoW**

No major deviation from the DoW have occurred.

## **Dissemination and uptake**

*The results of the Deliverable 1.4 have been disseminated outside the BACCHUS community by presentations at national and international conferences and workshops*

Ansmann, A., Bühl, J., Mamouri, R., Engelmann, R., Seifert, P., Nisantzi, A., Dadjimitsis, D. and Sciare, J.: Lidar observations of ice-nucleating particle (INPC) and ice crystal number (ICNC) concentrations: height-resolved INPC-ICNC closure studies in mixed-phase altocumulus layers, EGU, Vienna, Austria, 2017, oral presentation.

Bühl, J., P. Seifert, R. Engelmann, R. Mamouri, A. Nisantzi, B. Weinzierl, J. Sciare and A. Ansmann: First Results of the Cyprus Clouds Aerosols and Rain Experiment (CyCARE), Fifth International Conference on Remote Sensing and Geoinformation of Environment, Pafos, Cyprus, 2017.

Calmer, R., G. C. Roberts, and J. Preissler, S. Derrien, C. O'Dowd. 3D Wind Vector Measurements using a 5-hole Probe with Remotely Piloted Aircraft, Abstract for International Society for Atmospheric Research using Remotely piloted Aircraft, Oban, Scotland, 2017

Fiedler, S.: On the sensitivity of the effective radiative forcing of anthropogenic aerosol to the spatial shift of pollution between the 1970s and 2000s, AeroCom Workshop, Helsinki, Finland, 9.13. Oct. 2017.

Fossum, K. N., Ovadnevaite, J., Ceburnis, D. Dall'Osto, M., Marullo, S., Ballacicco, M., Simo, R., Zuend, A. and O'Dowd, C.: Aerosol physico-chemical and CCN properties in and around Antarctica during the austral summer, ICNAA conference, Helsinki, June 2017, poster presentation.

Gaita, S. M., Maier, Y., Boman, J., Gatari, M. J., Bingemer, H., Pettersson, J.B.C., Thomson, E. S.: Observations of a diurnal cycle of ice nucleating particle concentration on the shoulders of Mt. Kenya. ICNAA, Helsinki, Finland, June 25-30, 2017.

Herenz, P., Mangold, A., Wex, A. and Stratmann, F.: CCN measurements at the Princess Elisabeth Antarctica Research Station, ICCP 2016, poster presentation.

Kanji, Z. A. Atkinson, J. D., Siera, B. and Lohmann, U.: Ice Nucleating Particles around the world – a global review, EGU, Vienna, Austria, 2017, poster presentation.

Kinne, S.: Aerosol climatology – MACv2, AeroCom Workshop, Helsinki, Finland, 9.13. Oct. 2017.

Mangold, A., A. Delcloo, H. De Backer, Q. Laffineur, P. Herenz, H. Wex, A. Gossart, N. Souverijns, I. Gorodetskaya, and N. Van Lipzig: Aerosol and CCN properties at Princess Elisabeth station, East Antarctica: seasonality, new particle formation events and properties around precipitation events, EGU, Vienna, Austria, 2017, poster presentation.

Mangold, A., H. De Backer, Q. Laffineur, P. Herenz, H. Wex, A. Gossart, N. Souverijns, I. Gorodetskaya, and N. Van Lipzig: CCN and aerosol properties at Princess Elisabeth station, East Antarctica, combined with cloud and precipitation observations and air mass origin, EGU, Vienna, Austria, 2017, poster presentation.

Motos, G., J. Schmale, J.C. Corbin, M. Zanatta, U. Baltensperger and M. Gysel: Cloud condensation nuclei (CCN)-activation behaviour of atmospheric black carbon particles in fog as a function of their size and mixing state, European Aerosol Conference, Zurich, Switzerland, August 2017.

Motos, G., J. Schmale, J.C. Corbin, R. Modini, N. Karlen, E. Herrmann, U. Baltensperger and M. Gysel: Cloud condensation nuclei (CCN) activation behaviour of atmospheric black carbon in liquid clouds at the high-altitude site Jungfraujoch, Switzerland (3580m a.s.l.), Symposium on high altitude research, Gotemba, Japan, November 2017.

Ovadnevaite, J.: Nascent Ultra-Fine Marine Aerosol as Super-Efficient Cloud Nuclei, ICNAA conference, Helsinki, June 2017, oral presentation.

Rinaldi, M., Alessia Nicosia, Gianni Santachiara, Stefano Decesari, Marco Paglione, Silvia Sandrini, Stefania Gilardoni, Paolo Cristofanelli, Angela Marinoni, Paolo Bonasoni, Maria Cristina Facchini, and Franco Belosi: Ice Nuclei measurements across Europe within BACCHUS, EGU, Vienna, Austria, 2017, poster presentation.

Roberts, G.C., R. Calmer, K. Sanchez, S. Lauda, V. Brunaud, K. Nicoll, J. Ovadnevaite, D. Ceburnis, D. Rosenfeld, multi-dimensional Cloud-aERosol Exploratory Study, Abstract for International Society for Atmospheric Research using Remotely piloted Aircraft, Toulouse, France, 2016

Rosenfeld, D., Aircraft measured vertical profiles of cloud microstructure and precipitation initiation under contrasting aerosol conditions over the Amazon, 5th iLEAPS Science Conference, 11-14 September 2017, Oxford, UK, session convener and presentation.

Rosenfeld, D., Anthropogenic aerosol cloud-mediated climate forcing: where are we with respect to the pristine background and how far from saturation?, Scientific symposium: Facts of Biogeochemistry, Max Planck Institute of Chemistry, Mainz, Germany, 19 May 2017, invited presentation.

Rosenfeld, D., CCN data from satellite retrievals and what can we do with them?, 5th AeroSAT workshop, 9-13 October 2017, Helsinki, Finland, invited presentation.

Rosenfeld, D., Clouds Obscuring Aerosol Retrievals? Using Clouds for Revealing Aerosol Emission Sources and Climatic Impacts, Gordon Research Conference on Atmospheric Chemistry, 30 July - 4 August 2017, Sunday River, Maine, USA, invited presentation.

Rosenfeld, D., The profound role of CN in substantial invigoration of deep tropical convective clouds with active warm rain processes: observations and simulations, GEWEX Aerosol Precipitation (GAP) initiative workshop on aerosol effects on precipitation. 28-30 June 2017, Oxford, UK, invited presentation.

Rosenfeld, D., Towards Satellite Retrievals of Cloud Base CCN and Updrafts - The Greatest Observational Needs in Aerosol-Cloud Interactions, annual meeting of the American Meteorological Society, 22-26 January 2016, Seattle, Invited presentation in the 19th Conference on Atmospheric Chemistry.

Schmale, J. et al. (> 50 co-authors): What do we learn from long-term CCN observations? European Aerosol Conference, Zurich, Switzerland, August 2017

Schmale, J., S. Henning, A. Baccarini, F. Tunmon, M. Hartman, A. Welti, J. Dommen, F. Stratmann, C. Bolas, N. Harris, D. Rosenfeld, K. Carslaw, M. Schnaiter, A. Prevot, U. Baltensperger, M. Gysel: In search of the preindustrial atmosphere, Globalizing Polar Issues Conference, Crans-Montana, Switzerland, September 2017

Schmale, J., S. Henning, A. Baccarini, F. Tunmon, M. Hartman, A. Welti, J. Dommen, F. Stratmann, C. Bolas, N. Harris, D. Rosenfeld, K. Carslaw, M. Schnaiter, A. Prevot, U. Baltensperger, M. Gysel: Overview of aerosol and trace gases measurements during the Antarctic Circumnavigation Expedition 2016-2017, European Aerosol Conference, Zurich, Switzerland, August 2017

Schmale, J.: Air Pollution and Arctic Change: Past, Present and Future Challenges, Arctic Circle, Reykjavik, Iceland, October 2017

Schmale, J.: Antarctic Circumnavigation Expedition: In search of the pristine atmosphere, Swiss Embassy to the EU, Brussels, Belgium, 26 April, 2017

Schmale, J.: Antarctic Circumnavigation Expedition: In search of the pristine atmosphere, Eidgenössische Forschungsanstalt für Wald Schnee und Landschaft, Birmensdorf, December 1, 2016.

Schmale, J.: The Antarctic Circumnavigation Expedition: Studying the Southern Ocean and Antarctica, Paul Scherrer Institute Colloquium, 10.11.2017

Schmale, J.: The Antarctic Circumnavigation Expedition: Studying the Southern Ocean and Antarctica, University of Leeds, Colloquium, 21.11.2017

Schmale, J.: The Antarctic Circumnavigation Expedition: Studying the Southern Ocean and Antarctica, ETH Zurich, Versuchsanstalt für Wasserbau, 30.11.2017

Schrod, J., Weber, D., Thomson, E. S., Pöhlker, C., Saturno, J., Artaxo, P., Curtius, J. and Bingemer, H. G.: Ice nucleating particles from a large-scale sampling network: insight into geographic and temporal variability, EGU, Vienna, Austria, 2017, poster presentation.

Thomson, E.S.: Cloud Particle Formation: fundamentals and fun! Interdisciplinary Workshop on Biophysical Atmospheric Processes, Sven Lovèn Marine Center, Kristineberg, Sweden, Nov. 1-3, 2017.

Vergara-Temprado, J., Murray, B.J., Wilson, T. W., O'Sullivan, D., Browse, J. Pringle, K. J., Ardon-Dryer, K., Bertram, A. K., Burrows, S. Cerbunis, D., DeMott, P. J., Mason, R. H., O'Dowd, C. D., Rinaldi, M., Carslaw, K. S.; Contribution of Feldspar and Marine Organic aerosols to global ice nucleating particle concentrations, EGU, Vienna, Austria, 2017, oral presentation.

Weber, D., Schrod, J., Drücke, J., Keleshis, C., Pikriday, M., Ebert, M., Cvetkovic, B., Nickovix, S., Baars, H., Marinou, E., Vrekoussis, M., Sciare, J., Mihalopoulos, N., Curtius, J. and Bingemer, H. G.: Ice nucleating particles over the Eastern Mediterranean measured at ground and by unmanned aircraft systems, EGU, Vienna, Austria, 2017, oral presentation.

Welti, A. and Stratmann, F.: Frequency Distribution of Ambient Ice Nuclei Concentration, 1st Atmospheric Ice Nucleation Conference, Leeds 2017, oral Presentation.

Welti, A., Löffler, M., Stratmann, F.: Spatio-temporal variations in marine ice nuclei concentration, EGU, Vienna, Austria, 2017, poster presentation.

Main results have also been disseminated through published open-access articles and other publications and reports:

Belosi, F., Rinaldi, M., Decesari, S., Tarozzi, L., Nicosia, A., Santachiara, G.: Ground level ice nuclei particle measurements including Saharan dust events at a Po Valley rural site (San Pietro Capofiume, Italy), *Atmos. Res.*, 186, 116-126, 2017.

Braga, R. C., Rosenfeld, D., Weigel, R., Jurkat, T., Andreae, M. O., Wendisch, M., Pöhlker, M. L., Klimach, T., Pöschl, U., Pöhlker, C., Voigt, C., Mahnke, C., Borrmann, S., Albrecht, R. I., Molleker, S., Vila, D. A., Machado, L. A. T., and Artaxo, P.: Comparing parameterized versus measured microphysical properties of tropical convective cloud bases during the ACRIDICON-CHUVA campaign, *Atmos. Chem. Phys.*, 17, 7365-7386, <https://doi.org/10.5194/acp-17-7365-2017>, 2017.

Braga, R. C., Rosenfeld, D., Weigel, R., Jurkat, T., Andreae, M. O., Wendisch, M., Pöschl, U., Voigt, C., Mahnke, C., Borrmann, S., Albrecht, R. I., Molleker, S., Vila, D. A., Machado, L. A. T., and Grulich, L.: Aerosol concentrations determine the height of warm rain and ice initiation in convective clouds over the Amazon basin, *Atmos. Chem. Phys. Discuss.*, <https://doi.org/10.5194/acp-2016-1155>, in review, 2017.

Bucci, S., Cristofanelli, P., Decesari, S., Marinoni, A., Sandrini, S., Größ, J., Wiedensohler, A., Di Marco, C. F., Nemitz, E., Cairo, F., Di Liberto, L., and Fierli, F.: Vertical distribution of aerosol optical properties in the Po Valley during the 2012 summer campaigns, *Atmos. Chem. Phys. Discuss.*, <https://doi.org/10.5194/acp-2017-192>, in review, 2017.

Burkert-Kohn, M., Wex, H., Welti, A., Hartmann, S., Grawe, S., Hellner, L., Herenz, P., Atkinson, J. D., Stratmann, F., and Kanji, Z. A.: Leipzig Ice Nucleation chamber Comparison

(LINC): intercomparison of four online ice nucleation counters, *Atmos. Chem. Phys.*, 17, 11683-11705, <https://doi.org/10.5194/acp-17-11683-2017>, 2017.

Calmer, R., Roberts, G., Preissler, J., Derrien, S., and O'Dowd, C.: 3D Wind Vector Measurements using a 5-hole Probe with Remotely Piloted Aircraft, *Atmos. Meas. Tech. Discuss.*, <https://doi.org/10.5194/amt-2017-233>, in review, 2017.

Cecchini M. A., L. A. T. Machado, M. Wendisch, A. Costa, M. Krämer, M. O. Andreae, A. Afchine, R. I. Albrecht, P. Artaxo, S. Borrmann, D. Fütterer, T. Klimach, C. Mahnke, S. T. Martin, A. Minikin, S. Molleker, L. H. Pardo, C. Pöhlker, M. L. Pöhlker, U. Pöschl, D. Rosenfeld, B. Weinzierl, 2017: Illustration of microphysical processes in Amazonian deep convective clouds in the Gamma phase space: Introduction and potential applications. *Atmos. Chem. Phys. Discuss.*, doi:10.5194/acp-2017-185, in review, 2017.

Cecchini, M. A., Machado, L. A. T., Andreae, M. O., Martin, S. T., Albrecht, R. I., Artaxo, P., Barbosa, H. M. J., Borrmann, S., Fütterer, D., Jurkat, T., Mahnke, C., Minikin, A., Molleker, S., Pöhlker, M. L., Pöschl, U., Rosenfeld, D., Voigt, C., Weinzierl, B., and Wendisch, M.: Sensitivities of Amazonian clouds to aerosols and updraft speed, *Atmos. Chem. Phys.*, 17, 10037-10050, <https://doi.org/10.5194/acp-17-10037-2017>, 2017.

Dall'Osto, M., J. Ovadnevaite, M. Paglione, D. C. S. Beddows, D. Ceburnis, C. Cree, P. Cortés, M. Zamanillo, S. O. Nunes, G. L. Pérez, E. Ortega-Retuerta, M. Emelianov, D. Vaqué, C. Marrasé, M. Estrada, M. M. Sala, M. Vidal, M. F. Fitzsimons, R. Beale, R. Airs, M. Rinaldi, S. Decesari, M. Cristina Facchini, R. M. Harrison, C. O'Dowd, and R. Simó (2017), Antarctic sea ice region as a source of biogenic organic nitrogen in aerosols, *Scientific Reports*, 7(1), 6047, doi:10.1038/s41598-017-06188-x.

Decesari, S., Sowlat, M. H., Hasheminassab, S., Sandrini, S., Gilardoni, S., Facchini, M. C., Fuzzi, S., and Sioutas, C.: Enhanced toxicity of aerosol in fog conditions in the Po Valley, Italy, *Atmos. Chem. Phys.*, 17, 7721-7731, <https://doi.org/10.5194/acp-17-7721-2017>, 2017.

Eyal Hashimshoni, Eyal., Retrieval of CCN(S) in pristine environments as analogue to the pre-industrial era, Master Thesis, HUJI, 2017.

Fiedler, et al.: Chapter: Cruise MSM68/2 - Collecting Atmospheric Reference Data over Oceans (CARO), in booklet: Research Vessel Maria S. Merian, Cruises No. MSM68/2 – MSM70, Editor: Leitstelle Deutsche Forschungsschiffe, ISSN 1862-8869, 2017.

Fiedler, S.: Expedition booklet and two weekly reports from the Research Vessel Maria S. Merian by Chief Scientist S. Fiedler, Cruise 3.11-14.11.2017, <https://www.ldf.uni-hamburg.de/merian/wochenberichte.html>, 2017

Herenz, P., Wex, H., Henning, S., Kristensen, T. B., Rubach, F., Roth, A., Borrmann, S., Bozem, H., Schulz, H., and Stratmann, F.: Measurements of aerosol and CCN properties in the Mackenzie River delta (Canadian Arctic) during Spring-Summer transition in May 2014, *Atmos. Chem. Phys. Discuss.*, <https://doi.org/10.5194/acp-2017-745>, in review, 2017.

Kanji, Z.A., Ladino, L. A., Wex, H., Boose, Y., Burkert-Kohn, M., Cziczo, D. J., Krämer, M.: Overview of Ice Nucleating Particles, *Met. Monogr.*, 58, 1.1-1.3, <https://doi.org/10.1175/AMSMONOGRAPHSD-16-0006.1>, 2017.

Kinne, S.: Weekly Reports from the Research Vessel Sonne by Chief Scientist S. Kinne, Cruise 14.10.-4.11.2017, <https://www.ldf.uni-hamburg.de/sonne/wochenberichte.html>, 2017

Lacher, L., Lohmann, U., Boose, Y., Zipori, A., Herrmann, E., Bukowiecki, N., Steinbacher, M., and Kanji, Z. A.: The Horizontal Ice Nucleation Chamber HINC: INP measurements at Conditions Relevant for Mixed-Phase Clouds at the High Altitude Research Station Jungfraujoch, *Atmos. Chem. Phys. Discuss.*, <https://doi.org/10.5194/acp-2017-474>, in review, 2017.

Michaelides, Silas, Theodore Karacostas, Jose Luis Sánchez, Adrianos Retalis, Ioannis Pytharoulis, Víctor Homar, Romualdo, Romero, Prodromos Zanis, Christos Giannakopoulos,

Johannes, Bühl, Albert Ansmann, Andrés Merino, Pablo Melcón, Konstantinos Lagouvardos, Vassiliki Kotroni, Adriana Bruggeman, Juan Ignacio López-Moreno, Claude Berthet, Eleni Katragkou, Filippos Tymvios, Diofantos G. Hadjimitsis, Rodanthi-Elisavet Mamouri, Argyro Nisantzi: Reviews and perspectives of high impact atmospheric processes in the Mediterranean, *Atmos. Res.*, <https://doi.org/10.1016/j.atmosres.2017.11.022>, 2017

Preissler, J., G. Martucci, G. Saponaro, J. Ovadnevaite, A. Vaishya, P. Kolmonen, D. Ceburnis, L. Sogacheva, G. de Leeuw, and C. O'Dowd (2016), Six years of surface remote sensing of stratiform warm clouds in marine and continental air over Mace Head, Ireland, *J Geophys Res-Atmos*, 121(24), 14538-14557, doi:10.1002/2016JD025360.

Reddington, C. L., Carslaw, K. S., Stier, P., Schutgens, N., Coe, H., Liu, D., Allan, J., Browse, J., Pringle, K. J., Lee, L. A., Yoshioka, M., Johnson, J. S., Regayre, L. A., Spracklen, D. V., Mann, G. W., Clarke, A., Hermann, M., Henning, S., Wex, H., Kristensen, T. B., Leaitch, W. R., Pöschl, U., Rose, D., Andreae, M. O., Schmale, J., Kondo, Y., Oshima, N., Schwarz, J. P., Nenes, A., Andersson, B., Roberts, G. C., Snider, J. R., Leck, C., Quinn, P. K., Chi, X., Ding, A., Jimenez, J. L., and Zhang, Q.: The global aerosol synthesis and science project (GASSP): measurements and modeling to reduce uncertainty. *Bull. Am. Meteor. Soc.*, 98, 1857-1877, doi:10.1175/BAMS-D-15-00317.1, 2017.

Sanchez K. J., G. C. Roberts., R. Calmer, K. Nicoll, E. Hashimshoni, D. Rosenfeld, J. Ovadnevaite, J. Preissler, D. Ceburnis, C. O'Dowd, L. M. Russell, 2017: Top-down and Bottom-up aerosol-cloud-closure: towards understanding sources of uncertainty in deriving cloud radiative flux. *Atmos. Chem. Phys.*, 17, 9797-9814, <https://doi.org/10.5194/acp-17-9797-2017>, 2017.

Saponaro, G., Kolmonen, P., Sogacheva, L., Rodriguez, E., Virtanen, T., and de Leeuw, G.: Estimates of the aerosol indirect effect over the Baltic Sea region derived from 12 years of MODIS observations, *Atmos. Chem. Phys.*, 17, 3133-3143, <https://doi.org/10.5194/acp-17-3133-2017>, 2017.

Schmale, J., Henning, S., Decesari, S., Henzing, B., Keskinen, H., Paramonov, M., Sellegrí, K., Ovadnevaite, J., Pöhlker, M. L., Brito, J., Bougiatioti, A., Kristensson, A., Kalivitis, N., Stavroulas, I., Carbone, S., Jefferson, A., Park, M., Schlag, P., Iwamoto, Y., Aalto, P., Äijälä, M., Bukowiecki, N., Ehn, M., Frank, G., Fröhlich, R., Frumau, A., Herrmann, E., Herrmann, H., Holzinger, R., Kos, G., Kulmala, M., Mihalopoulos, N., Nenes, A., O'Dowd, C., Petäjä, T., Picard, D., Pöhlker, C., Pöschl, U., Poulain, L., Prévôt, A. S. H., Swietlicki, E., Andreae, M. O., Artaxo, P., Wiedensohler, A., Ogren, J., Matsuki, A., Yum, S. S., Stratmann, F., Baltensperger, U., and Gysel, M.: What do we learn from long-term cloud condensation nuclei number concentration, particle number size distribution, and chemical composition measurements at regionally representative observatories?, *Atmos. Chem. Phys. Discuss.*, <https://doi.org/10.5194/acp-2017-798>, in review, 2017.

Schmale, Julia, Henning, Silvia, Henzing, Bas, Keskinen, Helmi, Sellegrí, Karine, Ovadnevaite, Jurgita, Bougiatioti, Aikaterini, Kalivitis, Nikos, Stavroulas, Iasonas, Jefferson, Anne, Park, Minsu, Schlag, Patrick, Kristensson, Adam, Iwamoto, Yoko, Pringle, Kirsty, Reddington, Carly, Aalto, Pasi, Äijälä, Mikko, Baltensperger, Urs, Bialek, Jakub, Birmili, Wolfram, Bukowiecki, Nicolas, Ehn, Mikael, Fjæraa, Ann Mari, Fiebig, Markus, Frank, Göran, Fröhlich, Roman, Frumau, Arnoud, Furuya, Masaki, Hammer, Emanuel, Heikkinen, Liine, Herrmann, Erik, Holzinger, Rupert, Hyono, Hiroyuki, Kanakidou, Maria, Kiendler-Scharr, Astrid, Kinouchi, Kento, Kos, Gerard, Kulmala, Markku, Mihalopoulos, Nikolaos, Motos, Ghislain, Nenes, Athanasios, O'Dowd, Colin, Paramonov, Mikhail, Petäjä, Tuukka, Picard, David, Poulain, Laurent, Prévôt, André Stephan Henry, Slowik, Jay, Sonntag, Andre, Swietlicki, Erik, Svenningsson, Birgitta, Tsurumaru, Hiroshi, Wiedensohler, Alfred, Wittbom, Cerina, Ogren, John A., Matsuki, Atsushi, Yum, Seong Soo, Myhre, Cathrine Lund, Carslaw, Ken, Stratmann, Frank and Gysel, Martin: Collocated observations of cloud condensation nuclei, particle size distributions, and chemical composition, *Sci. Data*, 4, doi:10.1038/sdata.2017.3, 2017.

Schrod, J., Weber, D., Drücke, J., Keleshis, C., Pikridas, M., Ebert, M., Cvetković, B., Nickovic, S., Marinou, E., Baars, H., Ansmann, A., Vrekoussis, M., Mihalopoulos, N., Sciare, J., Curtius, J., and Bingemer, H. G.: Ice nucleating particles over the Eastern Mediterranean measured by unmanned aircraft systems, *Atmos. Chem. Phys.*, 17, 4817-4835, <https://doi.org/10.5194/acp-17-4817-2017>, 2017.

Stevens, B., Fiedler, S., Kinne, S., Peters, K., Rast, S., Müsse, J., Smith, S. J., and Mauritsen, T.: MACv2-SP: a parameterization of anthropogenic aerosol optical properties and an associated Twomey effect for use in CMIP6, *Geosci. Model Dev.*, 10, 433-452, <https://doi.org/10.5194/gmd-10-433-2017>, 2017.

Welti, A., Müller, K., Fleming, Z. L., and Stratmann, F.: Concentration and variability of ice nuclei in the subtropic, maritime boundary layer, *Atmos. Chem. Phys. Discuss.*, <https://doi.org/10.5194/acp-2017-783>, in review, 2017.

## Supplement

**Table 1S.** Seasonal and yearly (Y) cross-correlation between AOD, COT, Ref, LWP, alb, CTH and CF for different regions. Colors highlight some of correlation coefficients combinations (green for AOD & COT, yellow for AOD & CF, light blue for AOD & Ref, orange for AOD & LWP).

Table 1Sa. Amazon

seas	AOD	COT	Ref	LWP	alb	CTH	CF	
DJF	AOD	1	0,12	0,04	0,17	0,01	-0,03	0,3
DJF	COT	0,12	1	-0,02	0,27	0,78	0,07	0,1
DJF	Ref	0,04	-0,02	1	0,83	0,17	0,09	0,14
DJF	LWP	0,17	0,27	0,83	1	0,2	-0,03	0,33
DJF	Alb	0,01	0,78	0,17	0,2	1	0,11	0,14
DJF	CTH	-0,03	0,07	0,09	-0,03	0,11	1	0,29
DJF	CF	0,3	0,1	0,14	0,33	0,14	0,29	1
MAM	AOD	1	0,25	-0,07	-0,01	0,02	0,04	0,25
MAM	COT	0,25	1	-0,22	0,16	0,77	0,07	0,22
MAM	Ref	-0,07	-0,22	1	0,65	-0,01	0,07	0
MAM	LWP	-0,01	0,16	0,65	1	0,13	0,06	0,23
MAM	Alb	0,02	0,77	-0,01	0,13	1	0,05	0,22
MAM	CTH	0,04	0,07	0,07	0,06	0,05	1	0,34
MAM	CF	0,25	0,22	0	0,23	0,22	0,34	1
JJA	AOD	1	0,13	-0,02	0,16	0,1	0,09	0,42
JJA	COT	0,13	1	-0,22	0,23	0,77	0,09	0,2
JJA	Ref	-0,02	-0,22	1	0,62	-0,04	0,01	-0,05
JJA	LWP	0,16	0,23	0,62	1	0,22	0,03	0,31
JJA	Alb	0,1	0,77	-0,04	0,22	1	0,03	0,27
JJA	CTH	0,09	0,09	0,01	0,03	0,03	1	0,41
JJA	CF	0,42	0,2	-0,05	0,31	0,27	0,41	1
SON	AOD	1	0,17	-0,01	0,13	0,08	0,07	0,38
SON	COT	0,17	1	-0,13	0,21	0,77	0,07	0,16
SON	Ref	-0,01	-0,13	1	0,71	0,06	0,07	0,06
SON	LWP	0,13	0,21	0,71	1	0,18	0,02	0,27
SON	Alb	0,08	0,77	0,06	0,18	1	0,07	0,2
SON	CTH	0,07	0,07	0,07	0,02	0,07	1	0,34
SON	CF	0,38	0,16	0,06	0,27	0,2	0,34	1
Y	AOD	1	0,19	0	0,13	0,17	0,12	0,57
Y	COT	0,19	1	-0,14	0,17	0,77	0,06	0,08
Y	Ref	0	-0,14	1	0,64	0,04	0,1	0,1
Y	LWP	0,13	0,17	0,64	1	0,14	0,07	0,25
Y	Alb	0,17	0,77	0,04	0,14	1	0,06	0,13
Y	CTH	0,12	0,06	0,1	0,07	0,06	1	0,33
Y	CF	0,57	0,08	0,1	0,25	0,13	0,33	1

Table 1Sb. Europe

seas	AOD	COT	Ref	LWP	alb	CTH	CF	
DJF	AOD	1	-0,02	0,09	0,17	-0,12	0,15	0,16
DJF	COT	-0,02	1	-0,11	0,25	0,86	0,13	0,1
DJF	Ref	0,09	-0,11	1	0,67	-0,02	0,1	0,01
DJF	LWP	0,17	0,25	0,67	1	0,25	0,14	0,11
DJF	Alb	-0,12	0,86	-0,02	0,25	1	0,12	0,13
DJF	CTH	0,15	0,13	0,1	0,14	0,12	1	0,07
DJF	CF	0,16	0,1	0,01	0,11	0,13	0,07	1
MAM	AOD	1	0,13	-0,02	0,08	0,08	0,04	0,28
MAM	COT	0,13	1	-0,05	0,26	0,87	0,1	0,15
MAM	Ref	-0,02	-0,05	1	0,65	0	0,01	0
MAM	LWP	0,08	0,26	0,65	1	0,25	0,08	0,1
MAM	Alb	0,08	0,87	0	0,25	1	0,09	0,19
MAM	CTH	0,04	0,1	0,01	0,08	0,09	1	0,11
MAM	CF	0,28	0,15	0	0,1	0,19	0,11	1
JJA	AOD	1	0,31	0,04	0,18	0,27	0,01	0,44
JJA	COT	0,31	1	0,01	0,37	0,87	0,09	0,3
JJA	Ref	0,04	0,01	1	0,67	0,08	-0,02	-0,14
JJA	LWP	0,18	0,37	0,67	1	0,38	-0,01	0,12
JJA	Alb	0,27	0,87	0,08	0,38	1	0,07	0,3
JJA	CTH	0,01	0,09	-0,02	-0,01	0,07	1	0,24
JJA	CF	0,44	0,3	-0,14	0,12	0,3	0,24	1
SON	AOD	1	0,16	-0,01	0,19	0,09	0,06	0,25
SON	COT	0,16	1	-0,04	0,25	0,86	0,12	0,24
SON	Ref	-0,01	-0,04	1	0,66	0,04	0,05	0,02
SON	LWP	0,19	0,25	0,66	1	0,27	0,07	0,28
SON	Alb	0,09	0,86	0,04	0,27	1	0,12	0,27
SON	CTH	0,06	0,12	0,05	0,07	0,12	1	0,19
SON	CF	0,25	0,24	0,02	0,28	0,27	0,19	1
Y	AOD	1	0,22	0,05	0,18	0,2	0,02	0,37
Y	COT	0,22	1	-0,03	0,28	0,87	0,1	0,25
Y	Ref	0,05	-0,03	1	0,66	0,04	0,02	-0,06
Y	LWP	0,18	0,28	0,66	1	0,29	0,04	0,16
Y	Alb	0,2	0,87	0,04	0,29	1	0,09	0,27
Y	CTH	0,02	0,1	0,02	0,04	0,09	1	0,19
Y	CF	0,37	0,25	-0,06	0,16	0,27	0,19	1

Table 1Sc. China, land

seas		AOD	COT	Ref	LWP	alb	CTH	CF
DJF	AOD	1	0,2	-0,09	0,12	0,19	0,02	0,22
DJF	COT	0,2	1	0	0,43	0,89	0,11	0,16
DJF	Ref	-0,09	0	1	0,48	-0,01	0,32	-0,07
DJF	LWP	0,12	0,43	0,48	1	0,43	0,14	-0,02
DJF	Alb	0,19	0,89	-0,01	0,43	1	0,11	0,28
DJF	CTH	0,02	0,11	0,32	0,14	0,11	1	0,13
DJF	CF	0,22	0,16	-0,07	-0,02	0,28	0,13	1
MAM	AOD	1	0,1	-0,01	0,1	0,09	0,03	0,36
MAM	COT	0,1	1	-0,04	0,4	0,91	0,12	0,27
MAM	Ref	-0,01	-0,04	1	0,43	-0,09	0,29	-0,09
MAM	LWP	0,1	0,4	0,43	1	0,41	0,17	0,06
MAM	Alb	0,09	0,91	-0,09	0,41	1	0,17	0,35
MAM	CTH	0,03	0,12	0,29	0,17	0,17	1	0,2
MAM	CF	0,36	0,27	-0,09	0,06	0,35	0,2	1
JJA	AOD	1	-0,09	-0,08	0,02	-0,2	0,04	0,08
JJA	COT	-0,09	1	-0,18	0,25	0,92	0,15	0,33
JJA	Ref	-0,08	-0,18	1	0,32	-0,24	0,21	-0,1
JJA	LWP	0,02	0,25	0,32	1	0,29	-0,05	0,21
JJA	Alb	-0,2	0,92	-0,24	0,29	1	0,15	0,38
JJA	CTH	0,04	0,15	0,21	-0,05	0,15	1	0,36
JJA	CF	0,08	0,33	-0,1	0,21	0,38	0,36	1
SON	AOD	1	0,08	0,02	0,04	0,06	0,02	0,42
SON	COT	0,08	1	-0,34	0,24	0,9	0,18	0,35
SON	Ref	0,02	-0,34	1	0,27	-0,39	0,15	-0,27
SON	LWP	0,04	0,24	0,27	1	0,3	-0,04	0,15
SON	Alb	0,06	0,9	-0,39	0,3	1	0,19	0,4
SON	CTH	0,02	0,18	0,15	-0,04	0,19	1	0,38
SON	CF	0,42	0,35	-0,27	0,15	0,4	0,38	1
Y	AOD	1	0,01	0,01	0,11	-0,02	0	0,33
Y	COT	0,01	1	-0,23	0,31	0,91	0,11	0,31
Y	Ref	0,01	-0,23	1	0,48	-0,26	0,24	-0,21
Y	LWP	0,11	0,31	0,48	1	0,33	0,09	0,02
Y	Alb	-0,02	0,91	-0,26	0,33	1	0,13	0,38
Y	CTH	0	0,11	0,24	0,09	0,13	1	0,3
Y	CF	0,33	0,31	-0,21	0,02	0,38	0,3	1

Table 1Sd. China, ocean

seas		AOD	COT	Ref	LWP	alb	CTH	CF
DJF	AOD	1	-0,04	-0,24	-0,05	-0,03	0,07	0,33
DJF	COT	-0,04	1	0,01	0,31	0,91	0,05	0,35
DJF	Ref	-0,24	0,01	1	0,54	0,07	0,26	0,06
DJF	LWP	-0,05	0,31	0,54	1	0,32	0,18	0,23
DJF	Alb	-0,03	0,91	0,07	0,32	1	0,1	0,46
DJF	CTH	0,07	0,05	0,26	0,18	0,1	1	0,22
DJF	CF	0,33	0,35	0,06	0,23	0,46	0,22	1
MAM	AOD	1	0,08	-0,08	0,1	0,1	0,17	0,55
MAM	COT	0,08	1	0,24	0,44	0,91	0,03	0,3
MAM	Ref	-0,08	0,24	1	0,61	0,29	0,3	0,15
MAM	LWP	0,1	0,44	0,61	1	0,49	0,14	0,25
MAM	Alb	0,1	0,91	0,29	0,49	1	0,05	0,4
MAM	CTH	0,17	0,03	0,3	0,14	0,05	1	0,3
MAM	CF	0,55	0,3	0,15	0,25	0,4	0,3	1
JJA	AOD	1	-0,08	-0,19	0,07	-0,12	0,28	0,44
JJA	COT	-0,08	1	0,13	0,27	0,93	0,03	0,17
JJA	Ref	-0,19	0,13	1	0,75	0,13	0,18	0
JJA	LWP	0,07	0,27	0,75	1	0,22	0,08	0,1
JJA	Alb	-0,12	0,93	0,13	0,22	1	0,02	0,19
JJA	CTH	0,28	0,03	0,18	0,08	0,02	1	0,32
JJA	CF	0,44	0,17	0	0,1	0,19	0,32	1
SON	AOD	1	0,13	-0,31	0,04	0,1	0,07	0,46
SON	COT	0,13	1	0,06	0,27	0,9	0,07	0,25
SON	Ref	-0,31	0,06	1	0,64	0,08	0,12	-0,07
SON	LWP	0,04	0,27	0,64	1	0,28	0,08	0,08
SON	Alb	0,1	0,9	0,08	0,28	1	0,08	0,29
SON	CTH	0,07	0,07	0,12	0,08	0,08	1	0,36
SON	CF	0,46	0,25	-0,07	0,08	0,29	0,36	1
Y	AOD	1	0,01	-0,19	0,05	0	0,14	0,41
Y	COT	0,01	1	0,02	0,27	0,91	-0,06	0,3
Y	Ref	-0,19	0,02	1	0,63	0,05	0,31	0,03
Y	LWP	0,05	0,27	0,63	1	0,28	0,17	0,18
Y	Alb	0	0,91	0,05	0,28	1	-0,05	0,37
Y	CTH	0,14	-0,06	0,31	0,17	-0,05	1	0,26
Y	CF	0,41	0,3	0,03	0,18	0,37	0,26	1

Table 1Se. Atlantic

seas		AOD	COT	Ref	LWP	alb	CTH	CF
DJF	AOD	1	0,14	0,44	0,54	0,05	-0,15	0,2
DJF	COT	0,14	1	0,26	0,28	0,81	-0,14	0,02
DJF	Ref	0,44	0,26	1	0,96	0,04	-0,15	0,23
DJF	LWP	0,54	0,28	0,96	1	-0,18	-0,2	0,39
DJF	Alb	0,05	0,81	0,04	-0,18	1	-0,09	-0,07
DJF	CTH	-0,15	-0,14	-0,15	-0,2	-0,09	1	0,27
DJF	CF	0,2	0,02	0,23	0,39	-0,07	0,27	1
MAM	AOD	1	0,14	0,33	0,43	-0,01	-0,01	0,2
MAM	COT	0,14	1	0,28	0,3	0,84	-0,11	0,09
MAM	Ref	0,33	0,28	1	0,94	0,08	-0,04	0,27
MAM	LWP	0,43	0,3	0,94	1	-0,12	-0,14	0,45
MAM	Alb	-0,01	0,84	0,08	-0,12	1	-0,05	-0,02
MAM	CTH	-0,01	-0,11	-0,04	-0,14	-0,05	1	0,23
MAM	CF	0,2	0,09	0,27	0,45	-0,02	0,23	1
JJA	AOD	1	0,18	0,37	0,57	-0,03	-0,09	0,16
JJA	COT	0,18	1	0,28	0,29	0,83	-0,06	0,07
JJA	Ref	0,37	0,28	1	0,95	0,12	-0,01	0,19
JJA	LWP	0,57	0,29	0,95	1	-0,15	-0,12	0,37
JJA	Alb	-0,03	0,83	0,12	-0,15	1	-0,04	-0,03
JJA	CTH	-0,09	-0,06	-0,01	-0,12	-0,04	1	0,24
JJA	CF	0,16	0,07	0,19	0,37	-0,03	0,24	1
SON	AOD	1	0,16	0,27	0,37	0,03	-0,04	0,34
SON	COT	0,16	1	0,23	0,27	0,83	-0,03	0,11
SON	Ref	0,27	0,23	1	0,95	0,06	-0,09	0,12
SON	LWP	0,37	0,27	0,95	1	-0,17	-0,19	0,3
SON	Alb	0,03	0,83	0,06	-0,17	1	0	0,01
SON	CTH	-0,04	-0,03	-0,09	-0,19	0	1	0,23
SON	CF	0,34	0,11	0,12	0,3	0,01	0,23	1
Y	AOD	1	0,14	0,34	0,46	0	-0,07	0,24
Y	COT	0,14	1	0,26	0,28	0,82	-0,08	0,07
Y	Ref	0,34	0,26	1	0,95	0,08	-0,07	0,2
Y	LWP	0,46	0,28	0,95	1	-0,16	-0,16	0,38
Y	Alb	0	0,82	0,08	-0,16	1	-0,04	-0,02
Y	CTH	-0,07	-0,08	-0,07	-0,16	-0,04	1	0,24
Y	CF	0,24	0,07	0,2	0,38	-0,02	0,24	1

**Table 2S.: Seasonal and Yearly (Y) cross-correlation between AOD, COT, Ref, LWP, albedo(alb), CTH and CF for Atlantic, for different LWP ranges. Colors highlight some of correlation coefficients combinations (yellow for COT & albedo, blue for Ref & albedo).**

**Table 2Sa. LWP<25.**

seas		AOD	COT	Ref	LWP	alb	CTH	CF
DJF	AOD	1	-0,06	0,06	-0,03	-0,06	0,13	0,06
DJF	COT	-0,06	1	-0,2	0,9	0,99	-0,13	0,04
DJF	Ref	0,06	-0,2	1	0,13	-0,29	0,1	0
DJF	LWP	-0,03	0,9	0,13	1	0,87	-0,05	0,04
DJF	Alb	-0,06	<b>0,99</b>	<b>-0,29</b>	0,87	1	-0,14	0,04
DJF	CTH	0,13	-0,13	0,1	-0,05	-0,14	1	0,03
DJF	CF	0,06	0,04	0	0,04	0,04	0,03	1
MAM	AOD	1	-0,23	0,13	-0,16	-0,23	0,08	0,09
MAM	COT	-0,23	1	-0,25	0,86	0,99	-0,09	-0,01
MAM	Ref	0,13	-0,25	1	0,21	-0,34	0,09	0,07
MAM	LWP	-0,16	0,86	0,21	1	0,81	-0,03	0,04
MAM	Alb	-0,23	<b>0,99</b>	<b>-0,34</b>	0,81	1	-0,1	-0,01
MAM	CTH	0,08	-0,09	0,09	-0,03	-0,1	1	0,12
MAM	CF	0,09	-0,01	0,07	0,04	-0,01	0,12	1
JJA	AOD	1	-0,21	0,14	-0,14	-0,23	0,04	0,05
JJA	COT	-0,21	1	-0,27	0,84	0,99	-0,05	-0,13
JJA	Ref	0,14	-0,27	1	0,25	-0,36	0,09	0,08
JJA	LWP	-0,14	0,84	0,25	1	0,78	0,01	-0,08
JJA	Alb	-0,23	<b>0,99</b>	<b>-0,36</b>	0,78	1	-0,06	-0,13
JJA	CTH	0,04	-0,05	0,09	0,01	-0,06	1	-0,05
JJA	CF	0,05	-0,13	0,08	-0,08	-0,13	-0,05	1
SON	AOD	1	-0,12	0,11	-0,05	-0,13	0,1	0,14
SON	COT	-0,12	1	-0,22	0,84	0,99	0,01	-0,16
SON	Ref	0,11	-0,22	1	0,25	-0,32	0,06	0,05
SON	LWP	-0,05	0,84	0,25	1	0,78	0,05	-0,12
SON	Alb	-0,13	<b>0,99</b>	<b>-0,32</b>	0,78	1	0	-0,16
SON	CTH	0,1	0,01	0,06	0,05	0	1	0,05
SON	CF	0,14	-0,16	0,05	-0,12	-0,16	0,05	1
Y	AOD	1	-0,14	0,12	-0,07	-0,14	0,04	0,1
Y	COT	-0,14	1	-0,23	0,86	0,99	-0,05	-0,06
Y	Ref	0,12	-0,23	1	0,21	-0,33	0,08	0,06
Y	LWP	-0,07	0,86	0,21	1	0,81	0	-0,03
Y	Alb	-0,14	<b>0,99</b>	<b>-0,33</b>	0,81	1	-0,06	-0,07
Y	CTH	0,04	-0,05	0,08	0	-0,06	1	0,02
Y	CF	0,1	-0,06	0,06	-0,03	-0,07	0,02	1

**Table 2Sb. 25<LWP<50.**

seas		AOD	COT	Ref	LWP	alb	CTH	CF
DJF	AOD	1	-0,13	0,27	0,19	-0,18	0,04	0,08
DJF	COT	-0,13	1	-0,52	-0,03	0,94	-0,06	-0,11
DJF	Ref	0,27	-0,52	1	0,71	-0,73	0,01	0,23
DJF	LWP	0,19	-0,03	0,71	1	-0,27	0,09	0,26
DJF	Alb	-0,18	<b>0,94</b>	<b>-0,73</b>	-0,27	1	-0,06	-0,18
DJF	CTH	0,04	-0,06	0,01	0,09	-0,06	1	0,16
DJF	CF	0,08	-0,11	0,23	0,26	-0,18	0,16	1
MAM	AOD	1	-0,39	0,54	0,45	-0,48	0,07	0,09
MAM	COT	-0,39	1	-0,65	-0,31	0,96	0,02	-0,2
MAM	Ref	0,54	-0,65	1	0,84	-0,81	-0,09	0,37
MAM	LWP	0,45	-0,31	0,84	1	-0,51	-0,06	0,4
MAM	Alb	-0,48	<b>0,96</b>	<b>-0,81</b>	-0,51	1	0,05	-0,28
MAM	CTH	0,07	0,02	-0,09	-0,06	0,05	1	0,2
MAM	CF	0,09	-0,2	0,37	0,4	-0,28	0,2	1
JJA	AOD	1	-0,39	0,5	0,42	-0,46	0,01	0,09
JJA	COT	-0,39	1	-0,66	-0,34	0,96	-0,12	-0,26
JJA	Ref	0,5	-0,66	1	0,86	-0,82	0,04	0,38
JJA	LWP	0,42	-0,34	0,86	1	-0,53	0,01	0,37
JJA	Alb	-0,46	<b>0,96</b>	<b>-0,82</b>	-0,53	1	-0,1	-0,33
JJA	CTH	0,01	-0,12	0,04	0,01	-0,1	1	0,13
JJA	CF	0,09	-0,26	0,38	0,37	-0,33	0,13	1
SON	AOD	1	-0,32	0,33	0,22	-0,36	0,09	0,16
SON	COT	-0,32	1	-0,49	-0,09	0,93	-0,09	-0,06
SON	Ref	0,33	-0,49	1	0,78	-0,73	0,02	0,23
SON	LWP	0,22	-0,09	0,78	1	-0,34	0,02	0,28
SON	Alb	-0,36	<b>0,93</b>	<b>-0,73</b>	-0,34	1	-0,07	-0,15
SON	CTH	0,09	-0,09	0,02	0,02	-0,07	1	0,17
SON	CF	0,16	-0,06	0,23	0,28	-0,15	0,17	1
Y	AOD	1	-0,31	0,39	0,29	-0,37	0,05	0,13
Y	COT	-0,31	1	-0,58	-0,19	0,95	-0,05	-0,15
Y	Ref	0,39	-0,58	1	0,8	-0,77	-0,01	0,3
Y	LWP	0,29	-0,19	0,8	1	-0,41	0,02	0,33
Y	Alb	-0,37	<b>0,95</b>	<b>-0,77</b>	-0,41	1	-0,04	-0,23
Y	CTH	0,05	-0,05	-0,01	0,02	-0,04	1	0,17
Y	CF	0,13	-0,15	0,3	0,33	-0,23	0,17	1

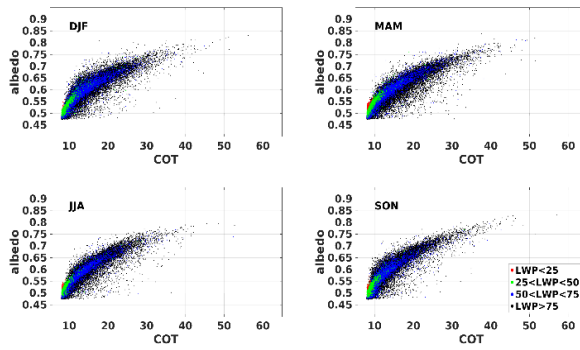
Table 2Sc.  $50 < LWP < 75$ .

seas		AOD	COT	Ref	LWP	alb	CTH	CF
DJF	AOD	1	0,06	0,09	0,08	0,03	-0,13	0,13
DJF	COT	0,06	1	0,12	0,13	0,92	-0,13	0,04
DJF	Ref	0,09	0,12	1	0,53	-0,09	-0,25	-0,08
DJF	LWP	0,08	0,13	0,53	1	0,05	-0,14	0,02
DJF	Alb	0,03	0,92	-0,09	0,05	1	-0,04	0,06
DJF	CTH	-0,13	-0,13	-0,25	-0,14	-0,04	1	0,25
DJF	CF	0,13	0,04	-0,08	0,02	0,06	0,25	1
MAM	AOD	1	-0,02	-0,06	-0,05	-0,03	0,17	0,18
MAM	COT	-0,02	1	0,16	0,27	0,93	-0,09	0,09
MAM	Ref	-0,06	0,16	1	0,54	-0,04	-0,09	-0,08
MAM	LWP	-0,05	0,27	0,54	1	0,24	-0,05	0,05
MAM	Alb	-0,03	0,93	-0,04	0,24	1	-0,06	0,12
MAM	CTH	0,17	-0,09	-0,09	-0,05	-0,06	1	0,18
MAM	CF	0,18	0,09	-0,08	0,05	0,12	0,18	1
JJA	AOD	1	0,07	0,06	0,12	0,05	0,01	0,22
JJA	COT	0,07	1	0,16	0,24	0,93	-0,14	0,04
JJA	Ref	0,06	0,16	1	0,54	-0,04	-0,09	-0,08
JJA	LWP	0,12	0,24	0,54	1	0,21	-0,06	0,05
JJA	Alb	0,05	0,93	-0,04	0,21	1	-0,12	0,06
JJA	CTH	0,01	-0,14	-0,09	-0,06	-0,12	1	0,16
JJA	CF	0,22	0,04	-0,08	0,05	0,06	0,16	1
SON	AOD	1	0,03	-0,01	0,06	0,02	0	0,31
SON	COT	0,03	1	0,01	0,1	0,93	-0,04	0,09
SON	Ref	-0,01	0,01	1	0,54	-0,2	-0,12	-0,08
SON	LWP	0,06	0,1	0,54	1	0,04	-0,1	0,04
SON	Alb	0,02	0,93	-0,2	0,04	1	0,02	0,11
SON	CTH	0	-0,04	-0,12	-0,1	0,02	1	0,18
SON	CF	0,31	0,09	-0,08	0,04	0,11	0,18	1
Y	AOD	1	0	-0,01	0,03	-0,01	0,03	0,22
Y	COT	0	1	0,12	0,19	0,93	-0,09	0,06
Y	Ref	-0,01	0,12	1	0,53	-0,08	-0,12	-0,08
Y	LWP	0,03	0,19	0,53	1	0,14	-0,08	0,04
Y	Alb	-0,01	0,93	-0,08	0,14	1	-0,05	0,09
Y	CTH	0,03	-0,09	-0,12	-0,08	-0,05	1	0,18
Y	CF	0,22	0,06	-0,08	0,04	0,09	0,18	1

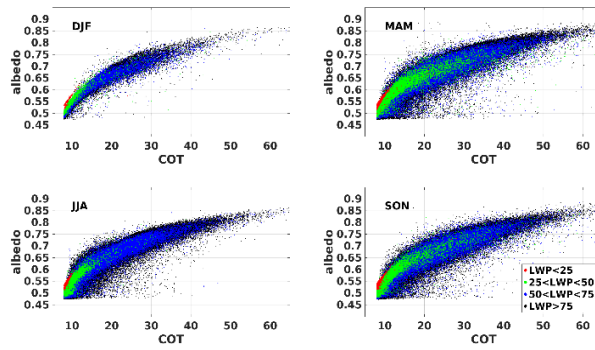
Table 2Sd.  $LWP > 75$ .

seas		AOD	COT	Ref	LWP	alb	CTH	CF
DJF	AOD	1	0,03	-0,06	0	0,05	0,12	0,22
DJF	COT	0,03	1	0,04	-0,01	0,92	-0,18	0,04
DJF	Ref	-0,06	0,04	1	0,54	-0,07	-0,08	0,06
DJF	LWP	0	-0,01	0,54	1	-0,05	0,05	-0,02
DJF	Alb	0,05	0,92	-0,07	-0,05	1	-0,16	0,05
DJF	CTH	0,12	-0,18	-0,08	0,05	-0,16	1	0,27
DJF	CF	0,22	0,04	0,06	-0,02	0,05	0,27	1
MAM	AOD	1	0,04	-0,08	-0,03	0,06	0,18	0,27
MAM	COT	0,04	1	0,03	0	0,93	-0,18	0,08
MAM	Ref	-0,08	0,03	1	0,6	-0,12	-0,05	-0,01
MAM	LWP	-0,03	0	0,6	1	-0,06	0,04	-0,04
MAM	Alb	0,06	0,93	-0,12	-0,06	1	-0,16	0,09
MAM	CTH	0,18	-0,18	-0,05	0,04	-0,16	1	0,23
MAM	CF	0,27	0,08	-0,01	-0,04	0,09	0,23	1
JJA	AOD	1	0,13	-0,07	-0,03	0,15	0,07	0,28
JJA	COT	0,13	1	0,02	0,01	0,93	-0,19	0,07
JJA	Ref	-0,07	0,02	1	0,61	-0,14	-0,02	-0,03
JJA	LWP	-0,03	0,01	0,61	1	-0,05	0,04	-0,05
JJA	Alb	0,15	0,93	-0,14	-0,05	1	-0,18	0,08
JJA	CTH	0,07	-0,19	-0,02	0,04	-0,18	1	0,22
JJA	CF	0,28	0,07	-0,03	-0,05	0,08	0,22	1
SON	AOD	1	0,13	-0,1	-0,05	0,16	0,08	0,41
SON	COT	0,13	1	-0,02	0,01	0,92	-0,14	0,1
SON	Ref	-0,1	-0,02	1	0,59	-0,18	-0,05	-0,03
SON	LWP	-0,05	0,01	0,59	1	-0,06	0,03	-0,01
SON	Alb	0,16	0,92	-0,18	-0,06	1	-0,12	0,11
SON	CTH	0,08	-0,14	-0,05	0,03	-0,12	1	0,19
SON	CF	0,41	0,1	-0,03	-0,01	0,11	0,19	1
Y	AOD	1	0,07	-0,08	-0,03	0,09	0,12	0,31
Y	COT	0,07	1	0,02	0	0,93	-0,17	0,08
Y	Ref	-0,08	0,02	1	0,59	-0,13	-0,05	-0,01
Y	LWP	-0,03	0	0,59	1	-0,05	0,04	-0,03
Y	Alb	0,09	0,93	-0,13	-0,05	1	-0,15	0,08
Y	CTH	0,12	-0,17	-0,05	0,04	-0,15	1	0,22
Y	CF	0,31	0,08	-0,01	-0,03	0,08	0,22	1

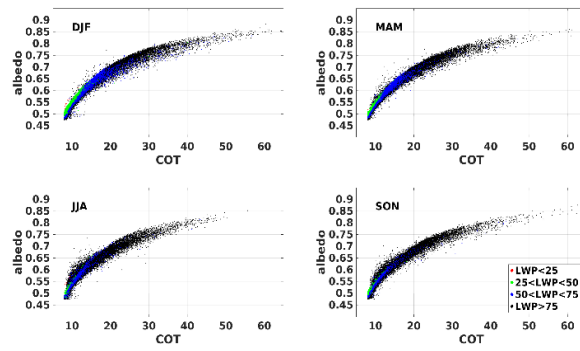
1Sa. Amazon



1Sb. Europe



1Sc. China, Land



1Sd. China, Ocean

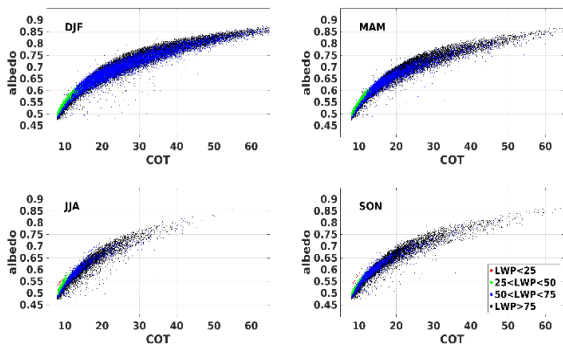
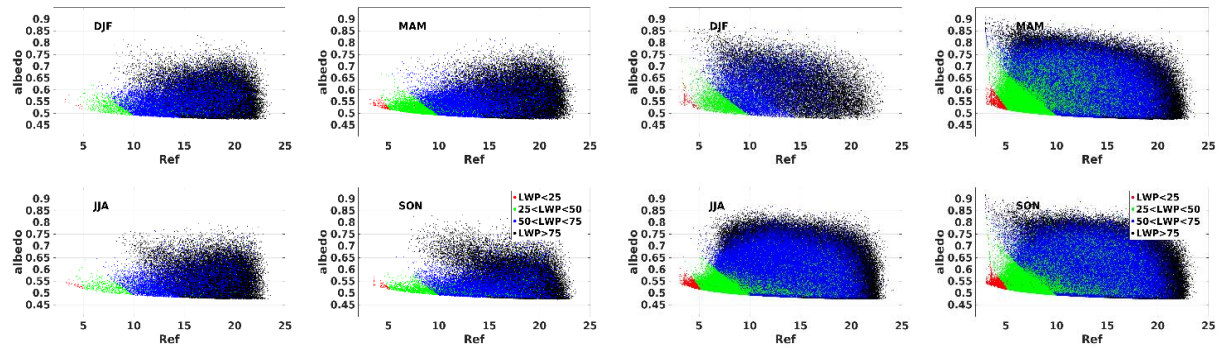
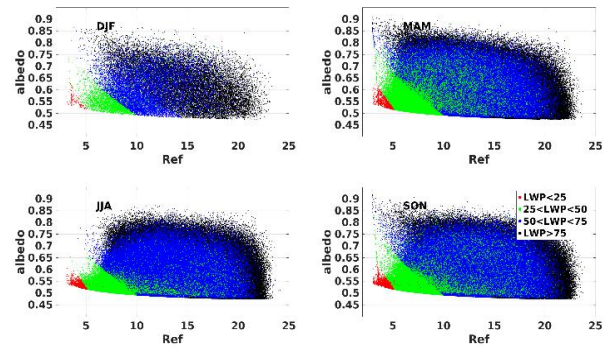


**Figure 1S.** COT and cloud albedo for LWP ranges (0-25-50-75-100) for different regions (Amazon (1Sa), Europe(1Sb), China Land(1Sc) and China ocean(1Sd) )and seasons (winter –DJF, spring –MAM, summer – JJA and Fall - SON).

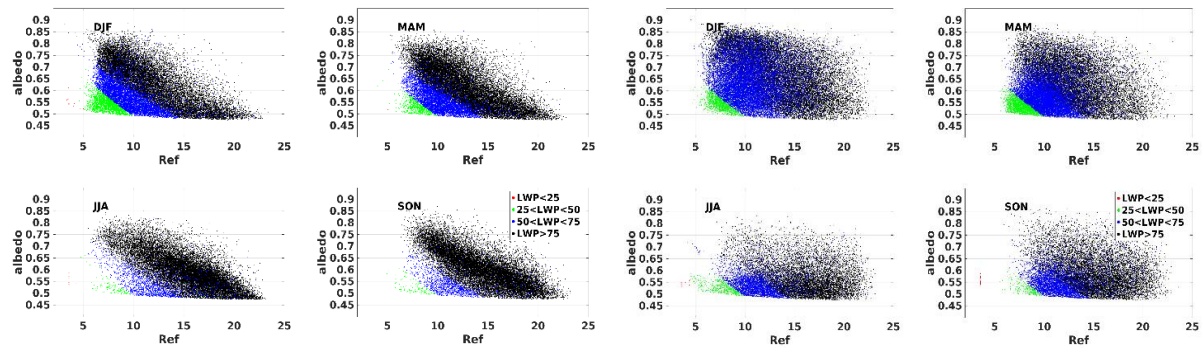
2Sa. Amazon



2Sb. Europe



2Sc. China, Land



2Sd. China, Ocean

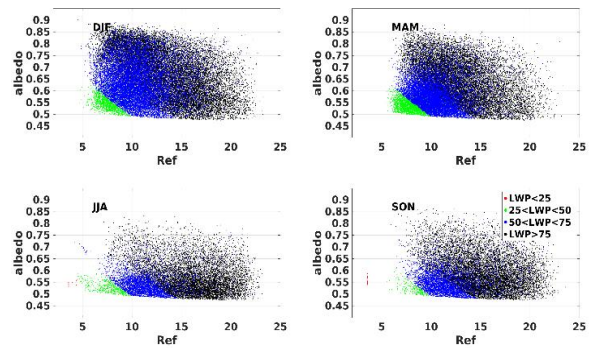


**Figure 2S.** Ref and cloud albedo for LWP ranges (0-25-50-75-100) for different regions (Amazon (1Sa), Europe(1Sb), China Land(1Sc) and China ocean(1Sd) )and seasons (winter –DJF, spring –MAM, summer – JJA and Fall - SON).